Petroleum Science 21 (2024) 1171–1189

Contents lists available at ScienceDirect

Petroleum Science

journal homepage: www.keaipublishing.com/en/journals/petroleum-science

Original Paper

A continuous and long-term in-situ stress measuring method based on fiber optic. Part I: Theory of inverse differential strain analysis

Kun-Peng Zhang [a, b, c], Mian Chen [a, b, *], Chang-Jun Zhao [a, b], Su Wang [a, b], Yong-Dong Fan [a, b]

[a] State Key Laboratory of Petroleum Resources and Prospecting, China University of Petroleum, Beijing, 102249, China
[b] MOE Key Laboratory of Petroleum Engineering in China University of Petroleum, Beijing, 102249, China
[c] Beijing International Center for Gas Hydrate, School of Earth and Space Sciences, Peking University, Beijing, 100871, China

ARTICLE INFO

Article history:
Received 31 December 2022
Received in revised form
9 October 2023
Accepted 9 October 2023
Available online 11 October 2023

Edited by Jia-Jia Fei

Keywords:
In-situ stress
Fiber optic
Orthotropic elastic
Differential evolution
ABAQUS

ABSTRACT

A method for in-situ stress measurement via fiber optics was proposed. The method utilizes the relationship between rock mass elastic parameters and in-situ stress. The approach offers the advantage of long-term stress measurements with high spatial resolution and frequency, significantly enhancing the ability to measure in-situ stress. The sensing casing, spirally wrapped with fiber optic, is cemented into the formation to establish a formation sensing nerve. Injecting fluid into the casing generates strain disturbance, establishing the relationship between rock mass properties and treatment pressure. Moreover, an optimization algorithm is established to invert the elastic parameters of formation via fiber optic strains. In the first part of this paper series, we established the theoretical basis for the inverse differential strain analysis method for in-situ stress measurement, which was subsequently verified using an analytical model. This paper is the fundamental basis for the inverse differential strain analysis method.

1. Introduction

In-situ stress is the basis of geomechanics (Zhang and Chen, 2022). It is pivotal in hydraulic fracturing and drilling engineering (Cong et al., 2022; Li et al., 2020; Zhang et al., 2020, 2021). Accurate and continuous in-situ stress profiles can significantly reduce engineering costs and risks (Zhang et al., 2022). In this way, the issue of in-situ stress measurement has received considerable critical attention.

Flat jack testing is one of the earliest in-situ stress measurement methods (Mayer et al., 1951). The flat jack is inserted into the wellbore and pressurized to sustain and measure the pressure acting on it. Hence, the method can only measure the stress perpendicular to the flat jack surfaces. He and Hatzor propose an analytical model for measuring three-dimensional in-situ stress using multiple flat jacks to overcome the shortcoming (He and Hatzor, 2015). However, inserting the flat jacks into the formation is difficult, especially at great depth.

Hydraulic fracturing testing is a proficient technique (Fairhurst, 1964) that enables precise measurement of the minimum horizontal in-situ stress (Haimson and Cornet, 2003). Treatment pressure data obtained from the process facilitates the inversion of in-situ stress. Many scholars have improved its accuracy (Cornet and Valette, 1984; Hayashi and Abe, 1984; Ito et al., 1999, 2006; Kuriyagawa et al., 1989; Serdyukov et al., 2016). Nevertheless, the measurement of the in-situ stress direction is relatively tricky.

The stress relief method is a standard in-situ measurement tool (Hast, 1967). The primary procedure is to drill holes in the wellbore and install strain gauges to record the holes' deformation. The strain data is used to invert the in-situ stress (Leeman and Hayes, 1966). However, performing the above operations in the wellbore is very challenging.

The Kaiser acoustic emission method is implemented on the rock mass unit (Hughson and Crawford, 1986). It is based on the theory that micro-fractures in the rock mass can store the stress history. The amplitude of the acoustic emission from the rock unit rises abruptly when the load exceeds the rock's historical maximum stress (Alhemdi and Gu, 2022; Chen et al., 2009; Ge et al.,

* Corresponding author.
E-mail address: chenm@cup.edu.cn (M. Chen).

https://doi.org/10.1016/j.petsci.2023.10.006

2015; Lu et al., 2011; Shi et al., 2004; Zhang et al., 2002). Similarly, the Differential Strain Analysis (DSA) is based on the memorability of rock micro-fractures (Emery, 1962). Hydrostatic pressure compresses the rock mass while the micro-fractures gradually close. The strain generated by the micro-fractures is used to calculate the in-situ stress ratio (Walsh, 1965). The main disadvantage of the DSA and Kaiser acoustic emission methods is that they both require coring from the formation, which cannot be performed directly downhole.

It is common to invert the in-situ stress via elastic parameters. Iverson proposes an inversion model based on the orthotropic Poisson's ratio (Iverson, 1995). The model assumes that no displacement or strain is generated within the formation under conditions of stress equilibrium. Then, the relationship between the in-situ stress and Poisson's ratio is established via the constitutive model. A continuous in-situ stress profile can be obtained based on the above model, combined with seismic and logging data (Gray D. et al., 2010, 2012; Gray F.D. et al., 2010a, b; Gray, 2013). The problem with the model is that the concept of stress is confusing. It is the change in stress that produces strain and displacement. However, strains and displacements will not be generated in a stress-equilibrium system. Therefore, the model assumptions are problematic.

The existing methods have the following disadvantages. On the one hand, a single measurement can only obtain the in-situ stress at a certain depth. Multiple measurements are required to obtain in-situ stress at different depths. It will significantly increase the cost and difficulty of measurement. On the other hand, a long-term in-situ stress measurement is difficult. Once the well is completed, measuring the in-situ stress is not easy. Hence, we proposed a method based on fiber optic sensing to solve the problems.

Fiber optic sensing is a promising sensing technology. Its advantages include high spatial resolution, accuracy, and frequency (Froggatt and Moore, 1998). The method, grounded in this technology, holds the potential to yield measurements across multiple depths through a singular measurement. The other advantage of the method is that the in-situ stress can be remeasured whenever needed since the sensing casing is cemented to the formation. In other words, the sensing casing can measure the dynamic strain of the formation. It enables long-term monitoring of the stresses in a structure (Kordell et al., 2022).

Consequently, the dynamic strain can invert critical parameters such as dynamic in-situ stress, flow rate, and temperature. Furthermore, if the sensing casing is deployed at multiple locations in the formation, it is equivalent to establishing a neural network. In this manner, important information, such as dynamic in-situ stress, temperature, and flow rate, can be obtained. The information can be shared within the formation neural network to obtain high-precision continuous information. If the network can be combined with big data and artificial technology, the network's capability can be further improved.

This work aims to establish the Inverse Differential Strain Analysis (IDSA) method. The first section of this paper will establish the theory of the IDSA. Moreover, a method for calculating the axial strain of fiber optic is established. Chapter 3 begins with an analytical model to simulate fracture deformation behavior and verifies the feasibility and performance of IDSA. Chapter 4 proposes the algorithm to invert the rock mass's elastic parameters. Chapter 5 verifies the algorithm's performance.

2. Theory of inverse differential strain analysis

The in-situ stress of a rock mass can be calculated using the IDSA method, which utilizes the orthotropic elastic parameters of the rock. IDSA generates dynamic strain in a rock mass through high-pressure fluid injection into the sensing casing, whereas DSA compresses the rock mass using hydrostatic pressure. The deformation behaviors resulting from the two methods are different. The basic theory of both IDSA and DSA are introduced in this chapter.

2.1. Differential strain analysis

DSA is one of the most important and effective means of in-situ stress measurement. The process of DSA is to implement the hydrostatic pressure to the rock mass unit. The strain is measured, as shown in Fig. 1. It should be noted that the unit is usually a cube with a side length (L) of 5 to 6 cm.

The DSA is based on the concept that rocks mass compression characteristics exhibit anisotropy caused by the rock mass's micro-fractures. Long-term compression within the formation establishes a direct relationship between the in-situ stress and micro-fractures (Carbillet et al., 2022). Therefore, these fractures' morphology and orientation are related to the in-situ stress. When the rock mass unit is subjected to in-situ stress, the micro-fractures are closed, and the rock mass remains isotropic elastic. However, when the in-situ stress is released after the rock mass unit is excavated, many micro-fractures in the rock mass are opened, resulting in anisotropic behavior.

The rock mass strain components are

$$\begin{cases} \varepsilon_{xx} = \left(\varepsilon_1^s + \varepsilon_9^s\right)/2 \\ \varepsilon_{yy} = \left(\varepsilon_6^s + \varepsilon_7^s\right)/2 \\ \varepsilon_{zz} = \left(\varepsilon_3^s + \varepsilon_4^s\right)/2 \\ \varepsilon_{xy} = \varepsilon_8^s - \left(\varepsilon_7^s + \varepsilon_9^s\right)/2 \\ \varepsilon_{xz} = \varepsilon_2^s - \left(\varepsilon_1^s + \varepsilon_3^s\right)/2 \\ \varepsilon_{yz} = \varepsilon_5^s - \left(\varepsilon_4^s + \varepsilon_6^s\right)/2 \end{cases} \tag{1}$$

where: $\varepsilon_1^s \sim \varepsilon_9^s$ - the rock mass strain measured by strain gages; ε_{ij} - rock mass strain components.

Fig. 2 displays the standard DSA test curve diagram. The slope of the curve depicts the effective compressibility of the rock mass.

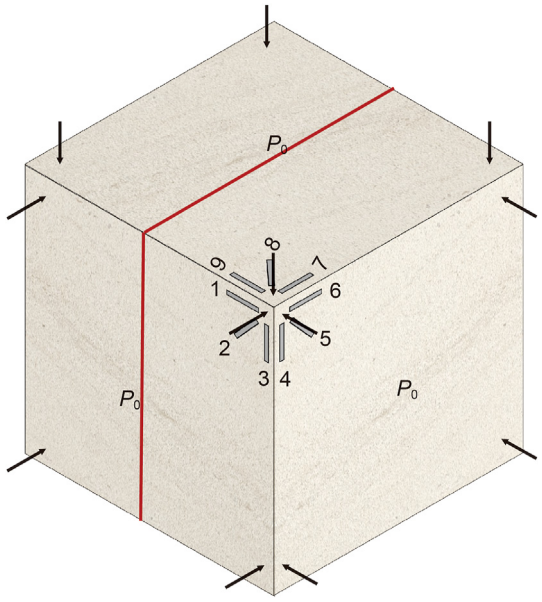

Fig. 1. DSA diagram. P_0 denotes the hydrostatic pressure exerted on the rock mass surface, while the red line symbolizes the in-situ stress signature line. The numbers denote the strain gauge attached to the surface.

Fracture stiffness and rock mass elastic modulus have an inverse relationship with the slope. Only fracture stiffness affects the effective compression coefficient, since the matrix elastic modulus is constant. Upon the release of in-situ stress, micro-fractures within the rock mass unit undergo expansion. Hydrostatic pressure causes micro-fractures in the rock mass to close, thereby decreasing its effective compressibility (Section OA). As micro-fractures reach full closure, the rock mass stiffness reaches a stable magnitude (Section AB). At this point, the rock mass unit behaves like an isotropic elastic material with constant elastic parameters.

The strain is divided into micro-fractures displacement and matrix strain, as follows

$$\varepsilon_{ij}^{\mathrm{DSA}} = \varepsilon_{ij}^{\mathrm{m}} + \varepsilon_{ij}^{\mathrm{f}} \tag{2}$$

where

$$\varepsilon_{ij}^{\mathrm{m}} = \begin{cases} \beta_{\mathrm{m}} P_0, & i = j = x, y, z \\ 0, & i \neq j \end{cases} \tag{3}$$

where superscripts DSA, m, and f refer to total strain, matrix strain, and fracture strain in DSA; β_{m} is the matrix effective compression coefficient.

The principal strain of micro-fractures strain is obtained by inserting Eqs. (1) and (2) into Eq. (3). And then, the principal stresses ratio is obtained as

$$\begin{cases} \sigma_{11} = \sigma_{33} \dfrac{(\upsilon(\varepsilon_{11} + \varepsilon_{33}) + (1-\upsilon)\varepsilon_{22})}{(\upsilon(\varepsilon_{11} + \varepsilon_{22}) + (1-\upsilon)\varepsilon_{33})} \\ \sigma_{22} = \sigma_{33} \dfrac{(\upsilon(\varepsilon_{22} + \varepsilon_{33}) + (1-\upsilon)\varepsilon_{11})}{(\upsilon(\varepsilon_{11} + \varepsilon_{22}) + (1-\upsilon)\varepsilon_{33})} \end{cases} \tag{4}$$

where: υ - Poisson's ratio of the rock mass matrix; ε_{11}, ε_{22}, ε_{33} - principal strains; σ_{11}, σ_{22}, σ_{33} - principal stresses.

Suppose the order of the in-situ stress magnitude is determined. In that case, the specific values of the in-situ stress are calculated using the density logging results. The in-situ stress direction can also be determined because it is consistent with the principal stress direction.

2.2. Inverse differential strain analysis

2.2.1. Internal pressurizing method

Like DSA, IDSA utilizes strain as a fundamental parameter to estimate in-situ stress. However, IDSA measures strain via the sensing casing comprising a fiber optic and shallowly grooved casing, as illustrated in Fig. 3.

The optical fiber is helically attached to the shallow slots. A film is attached outside the slots to shield the strain interference. Therefore, the fiber optic is only sensitive to the casing strain. The installation of the sensing casing is realized by cementing it into the formation.

The basis of IDSA is the inversion of the formation elastic parameters. What is more, the inversion is based on the strain. Unfortunately, a new equilibrium state will be formed relatively quickly when the wellbore is formed. In other words, fiber optics cannot sense the strain generated by the in-situ stress release. Therefore, a specific stress disturbance in the formation is necessary to cause sensible strains. In this way, the specificity of the rock mass to stress disturbance enabled the inversion of elastic parameters.

To implement stress disturbance, controllable and measurable stress is required. Thus, the Internal Pressurizing Method (IPM) is proposed, which involves injecting high-pressure fluid into the sensing casing to initiate stress disturbance. As shown in Fig. 4, a temporary packer is installed within the casing at both ends of the sensing section, and the high-pressure fluid is injected into the sealed section using pumping trucks. The formation around the sensing section is then subjected to radial expansion pressure and axial expansion tension. The strain of casing cemented in different rock masses under pressure is specific, enabling the inversion of elastic parameters of the rock mass by the casing strain under different pressures.

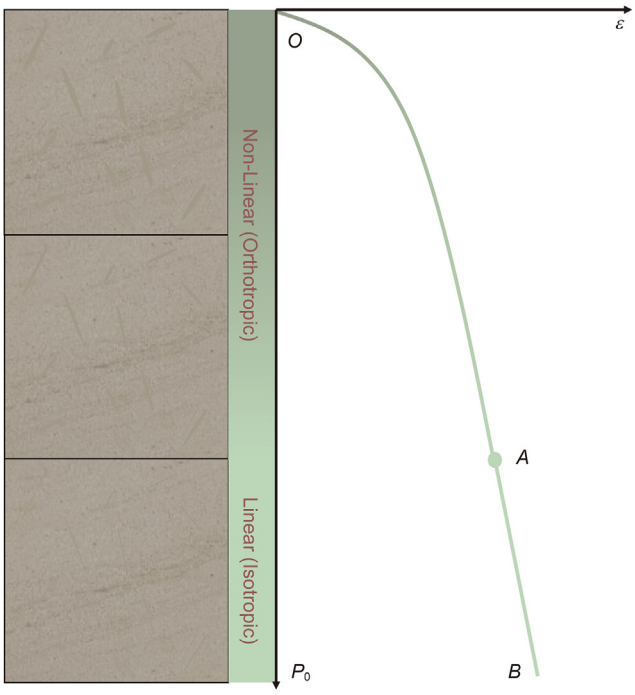

Fig. 2. DSA curve diagram. In Section OA, the micro-fractures are being gradually closed. Moreover, in Section AB, the micro-fractures are closed entirely.

2.2.2. Fiber optic axial strain conversion

Optical fibers only respond to strain along their longitudinal axis (Zheng et al., 2021). Consequently, it is imperative to transform spatial strain components into the axial strain of the optical fiber. As depicted in Fig. 5, the optical fiber is helically coiled on the external wall of the sensing casing.

Therefore, based on the helix equation, the spatial position coordinates parameter equation of the spiral fiber optic is

$$\begin{cases} x = -R\sin\theta \\ y = R\cos\theta \\ z = R\theta\tan\varphi \end{cases} \tag{5}$$

where: φ - helix angle; R - cylinder radius.

Eq. (5) is a parametric equation. The tangent equation of the fiber optic takes the form

$$\vec{V} = (x'(\theta), y'(\theta), z'(\theta)) \tag{6}$$

where: $\vec{V}$ - the fiber optic axial tangent vector, as shown in Fig. 5(a).

And the vector needs to be normalized to obtain the tangent vector as follows

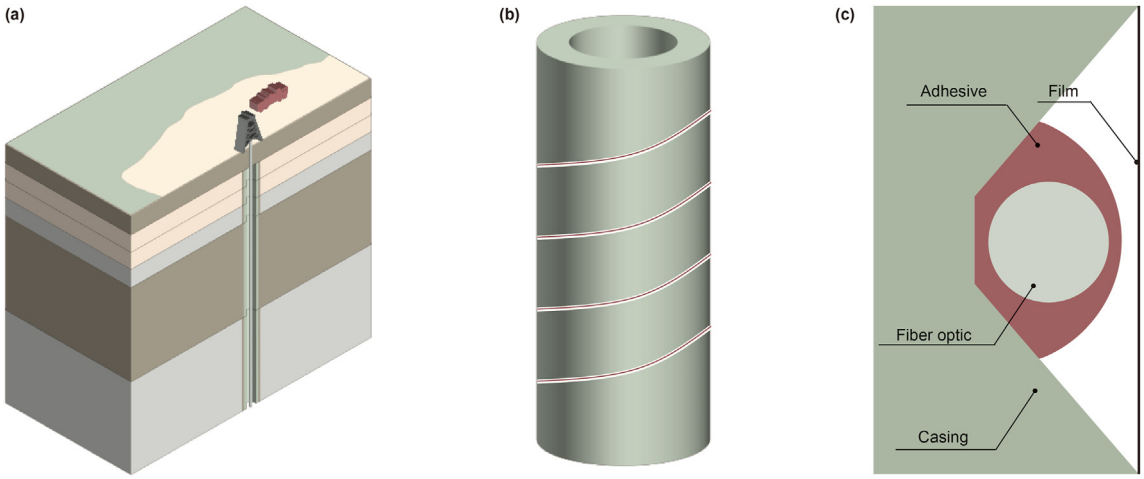

Fig. 3. Installation and structure diagram of sensing casing: (**a**) the sensing casing installed into the formation; (**b**) sensing casing structure. The white line represents the shallow helix slots, the red curve represents the fiber optic stuck to the slots; (**c**) the details of the sensing casing.

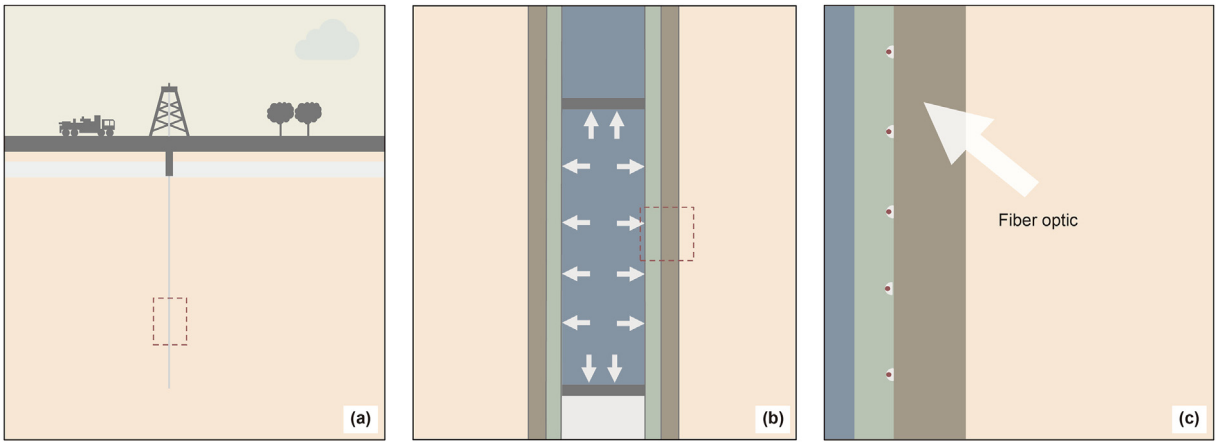

Fig. 4. Diagram of IPM: (**a**) the overall preview of IPM; (**b**) the pressurized section; (**c**) the partially enlarged view of the sensing casing.

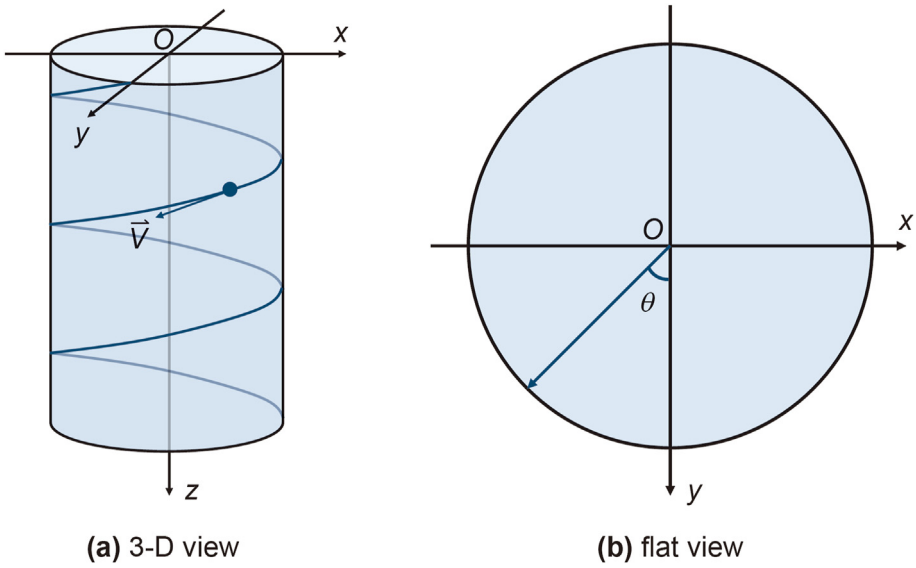

Fig. 5. Spiral wound fiber optic.

$$\vec{T} = \vec{V} \Big/ \left|\vec{V}\right| = (l, m, n) \tag{7}$$

where the direction cosine l, m, and n are

$$\begin{cases} l = -\cos\theta\left(1 + \tan^2\varphi\right)^{-1/2} \\ m = -\sin\theta\left(1 + \tan^2\varphi\right)^{-1/2} \\ n = \tan\varphi\left(1 + \tan^2\varphi\right)^{-1/2} \end{cases} \tag{8}$$

Then, the tangential strain along the fiber optic axis is calculated as follows

$$\varepsilon_N = l^2\varepsilon_x + m^2\varepsilon_y + n^2\varepsilon_z + lm\gamma_{xy} + mn\gamma_{yz} + ln\,\gamma_{xz} \tag{9}$$

2.2.3. Theory of IDSA

The in-situ stress in a rock mass can be measured using IDSA, which relies on the elastic parameters of the rock mass. This method uses fiber optic technology to connect the rock mass parameters with the casing's internal pressure. However, once the wellbore is created, the stress disturbance caused by the in-situ stress release dissipates rapidly. To better comprehend this process, a numerical simulation is conducted using ABAQUS.

The model is shown in Fig. 6. The parameters are listed in Table 1, where subscripts c and s refer to casing and cement sheath. E refers to rock mass elastic modulus.

The simulation utilizes a predefined field for the in-situ stress. The birth-death element eliminates the rock surrounding the borehole once the in-situ stress attains equilibrium. The stress caused by this compression compresses the rock surrounding the borehole, resulting in over-compressed micro-fractures around it, as displayed in Fig. 7(a)–(c).

The internal pressure will be applied within the casing to generate strain disturbance after the sensing casing is cemented.

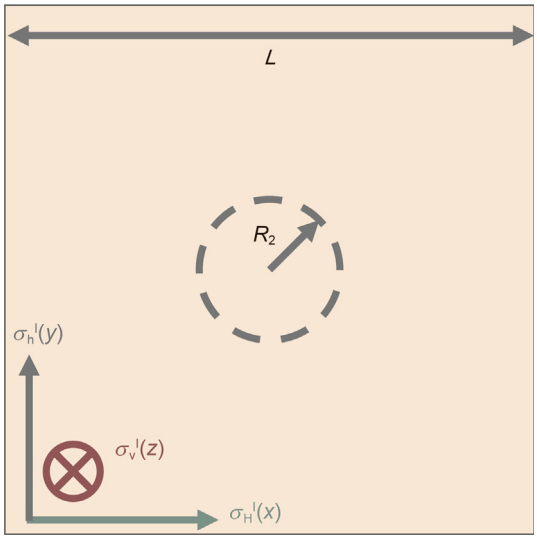

Fig. 6. Borehole model diagram. The borehole will be located in the area surrounded by dotted lines. The area will be removed through the birth-death element.

Table 1
Numerical model parameters.

Parameters	Values	Parameters	Values
E_c, GPa	210	R_0, mm	34
υ_c	0.304	R_1, mm	37
E_s, GPa	5	R_2, mm	42
υ_s	0.24	L, mm	300
E	50	σ_H^I, MPa	25
υ	0.24	σ_h^I, MPa	15
P_0, MPa	100	σ_v^I, MPa	20

Then, a numerical simulation is conducted to simulate the process. The model is shown in Fig. 14(a) and (b). The parameters are listed in Table 1. The results are shown in Fig. 7(d)–(f). The casing and the formation will be expended after the pressure is implemented. The formation of circumferential tensile strain around the wellbore is evident, as displayed in Fig. 7, with a gradual expansion of over-compressed micro-fractures.

In-situ stress release and IPM are opposite processes for micro-fractures. The schematic diagram of the IDSA test is shown in Fig. 8. In Section OA, micro-fractures are over-compressed, and the rock mass is isotropic. Gradual expansion of micro-fractures occurs in Section AB, causing the rock mass to become anisotropic with variable elastic parameters. Micro-fractures enhance compressibility and reduce the rock mass's elastic modulus, consistent with DSA theory.

In Section BC, the micro-fractures are fully opened. Then, the rock mass is an orthotropic elastic material with constant elastic parameters. It should be noted that the rock mass will not be fractured by the expansion pressure to protect the rock mass. The deformation behavior of IDSA is consistent with that of the rock mass tensile test (Zeng et al., 2019).

In IDSA, the following assumptions are made:

(1) The inherent anisotropy of the formation is not considered. That is, the rock matrix is isotropic elastic.
(2) Micro-fractures in the formation can be opened and closed due to stress.
(3) The existence of micro-fractures causes rock mass to be anisotropic.
(4) The anisotropic rock mass is simplified as orthotropic.
(5) The micro-fractures can be regarded as entirely healed and do not influence the elastic parameters of formation when the micro-fractures are closed to a certain extent.
(6) It can be considered that there are no micro-fractures in the rock mass when the number of healed micro-fractures reaches a specific value. Meanwhile, the rock mass is isotropic elastic.
(7) Plastic deformation and failure behavior are not considered.
(8) The micro-fractures are in a fully expanded state and will not continue to be expanded when the micro-fractures are opened to a certain extent.
(9) It can be considered that the rock mass orthotropic elastic parameters are constant when the number of fully expanded micro-fractures reaches a specific magnitude.
(10) The effect of coupling fields, such as pore pressure and thermal stress, is ignored.

Based on the IDSA test, the elastic parameters of rock mass and matrix can be obtained via the method introduced in Chapter 4.

Given the elastic parameters acquired via the IDSA test, a

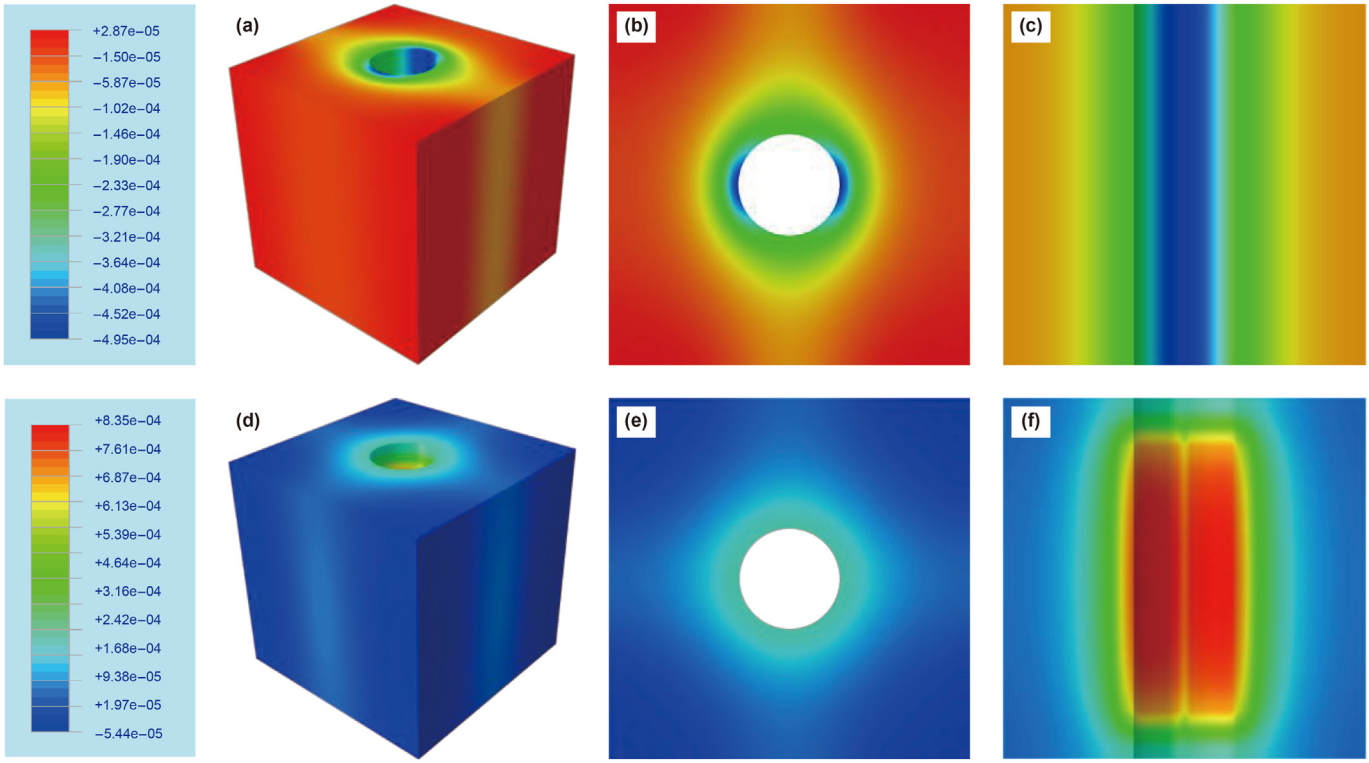

Fig. 7. Numerical simulation results of circumferential strain. Results of in-situ stress release (**a**–**c**) and inter-pressurizing (**d**–**f**) are presented. 3-D views are shown for (**a**) and (**d**), while (**b**) and (**e**) are top views, and (**c**) and (**f**) are cutaway views. Notably, (**d**–**f**) intentionally hides the casing and cement sheath to clearly show the borehole.

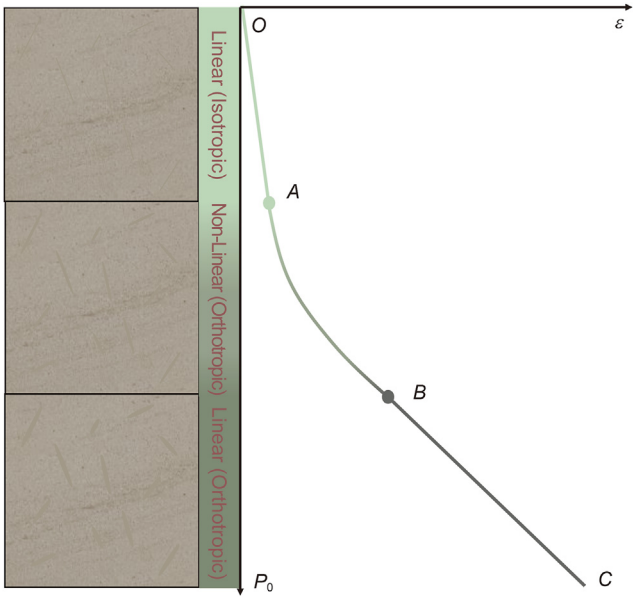

Fig. 8. IDSA schematic diagram. From points O to C, the state of fractures can be divided into three categories. They are over-compressed, partially opened, and entirely opened.

simulated virtual rock mass may be constructed for the DSA test. Under the hydrostatic pressure P_0, the rock mass strains are

$$\begin{cases} \varepsilon_{xx} = -P_0(1-\upsilon_{12}-\upsilon_{13}) \\ \varepsilon_{yy} = -P_0E_2^{-1}(1-\upsilon_{21}-\upsilon_{23}) \\ \varepsilon_{zz} = -P_0E_3^{-1}(1-\upsilon_{31}-\upsilon_{32}) \\ \varepsilon_{xy} = \varepsilon_{xz} = \varepsilon_{yz} = \varepsilon_{yx} = \varepsilon_{zx} = \varepsilon_{zy} = 0 \end{cases} \tag{10}$$

where: E_i - orthotropic elastic modulus; υ_{ij} - orthotropic Poisson's ratio. And the relationship between the elastic parameters is

$$\begin{cases} \upsilon_{12}E_2 = \upsilon_{21}E_1 \\ \upsilon_{13}E_3 = \upsilon_{31}E_1 \\ \upsilon_{23}E_3 = \upsilon_{32}E_2 \end{cases} \tag{11}$$

As per the principle of strain superposition, rock mass deformation can be partitioned into two components: micro-fractures and matrix strain. Certain equations give the mathematical expressions representing these components

$$\begin{cases} \varepsilon_{xx} = \varepsilon_{xx}^{\mathrm{m}} + \varepsilon_{xx}^{\mathrm{f}} \\ \varepsilon_{yy} = \varepsilon_{yy}^{\mathrm{m}} + \varepsilon_{yy}^{\mathrm{f}} \\ \varepsilon_{zz} = \varepsilon_{zz}^{\mathrm{m}} + \varepsilon_{zz}^{\mathrm{f}} \end{cases} \tag{12}$$

where the superscripts m and f denote the rock matrix and micro-fractures, and

$$\varepsilon_{xx}^{\mathrm{m}} = \varepsilon_{yy}^{\mathrm{m}} = \varepsilon_{zz}^{\mathrm{m}} = -(1-2\upsilon)P_0/E \tag{13}$$

Substituting from Eqs. (10) and (12) into Eq. (13) give the micro-fracture's principal strain as follows

$$\begin{cases} \varepsilon_{11} = -P_0((1-\upsilon_{12}-\upsilon_{13})/E_1 - (1-2\upsilon)/E) \\ \varepsilon_{22} = -P_0((1-\upsilon_{21}-\upsilon_{23})/E_2 - (1-2\upsilon)/E) \\ \varepsilon_{33} = -P_0((1-\upsilon_{32}-\upsilon_{311})/E_3 - (1-2\upsilon)/E) \end{cases} \tag{14}$$

As with the DSA method, the ratio of principal stress (in-situ stress) can be calculated by Eqs. (4) and (14). The principal stress direction is consistent with the direction of the principal elastic axis. In other words, the in-situ stress direction is consistent with the direction of the principal elastic axis (Alhemdi and Gu, 2022).

3. Verification of IDSA

3.1. Mathematical model of rock mass mechanical behavior

The rock mass comprises numerous structural surfaces, including natural micro-fractures and cleavages. Fig. 9 illustrates that the deformation of the rock mass is categorized into the matrix and structural surface deformation, with the structural surface collectively termed as micro-fracture for convenience. However, it is noteworthy that the model solely characterizes the deformation behavior of micro-fractures under compression and is not entirely applicable to rocks under tension.

In general, the micro-fracture deformation is described by the stress-displacement model. The stress and displacement are normal or tangential, as shown in Fig. 10.

3.1.1. Micro-fractures normal displacement

The deformation resistance of micro-fractures is assessed through their fracture stiffness, which is influenced by the normal stress exerted on them. As the normal stress increases, the distance between the upper and lower surfaces of micro-fractures decreases, resulting in a higher fracture stiffness and greater rock mass deformation resistance. When the normal stress surpasses the normal stress limit (σ_{nmax}), the fracture will no longer deform. The micro-fracture's normal stiffness is evaluated as follows (Zhang, 2006)

$$K_{\mathrm{n}}^{i} = K_{\mathrm{n0}}^{i}\left(\sigma_{\mathrm{nmax}}^{i}\right)^{2}\left(\sigma_{\mathrm{n}}^{i} - \sigma_{\mathrm{nmax}}^{i}\right)^{-2} \tag{15}$$

where: K_{n}^{i} - normal stiffness; K_{n0}^{i} - initial normal stiffness.

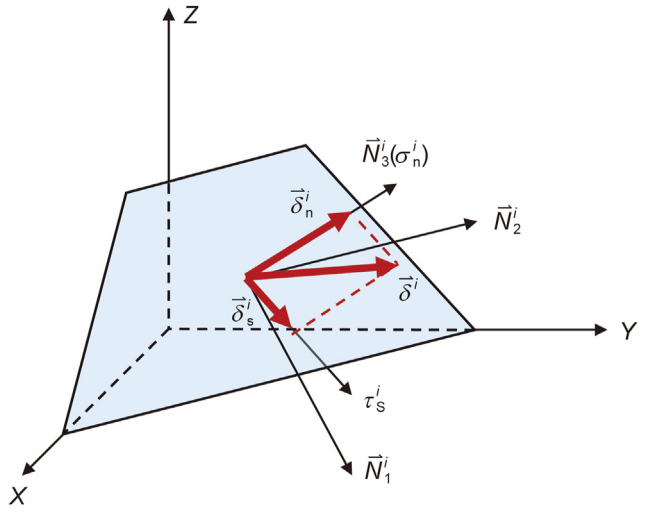

Fig. 10. Stress and displacement diagram of the i-th micro-fracture. $\delta_{\mathbf{i}}$, $\delta_{\mathbf{n}}^{\boldsymbol{i}}$, and $\delta_{\mathbf{s}}^{\boldsymbol{i}}$ are total displacement, normal displacement, and tangential displacement. $\boldsymbol{\sigma}_{\mathbf{n}}^{\boldsymbol{i}}$ and $\boldsymbol{\tau}_{\mathbf{s}}^{\boldsymbol{i}}$ are normal stress and shear stress. $\boldsymbol{N}_{\mathbf{1}}^{\boldsymbol{i}}$, $\boldsymbol{N}_{\mathbf{2}}^{\boldsymbol{i}}$, and $\boldsymbol{N}_{\mathbf{3}}^{\boldsymbol{i}}$ are the coordinate base vectors of the fracture's local coordinate system.

The relationship between δ_{n} and σ_{n} is

$$\mathrm{d}\delta_{\mathrm{n}}^{i} = \mathrm{d}\sigma_{\mathrm{n}}^{i} \Big/ K_{\mathrm{n}}^{i} \tag{16}$$

Combining Eqs. (15) and (16), and integrating from zero to σ_{nmax} for σ_{n}, an explicit relationship between δ_{n} and σ_{n} is obtained as follows

$$\delta_{\mathrm{n}}^{i} = \begin{cases} \left(\sigma_{\mathrm{n}}^{i} - \sigma_{\mathrm{nmax}}^{i}\right)^{3} \Big/ \left(3K_{\mathrm{n0}}^{i}\left(\sigma_{\mathrm{nmax}}^{i}\right)^{2}\right) + \sigma_{\mathrm{nmax}}^{i} \Big/ \left(3K_{\mathrm{n0}}^{i}\right), \sigma_{n}^{i} > \sigma_{\mathrm{nmax}}^{i} \\ \sigma_{\mathrm{nmax}}^{i} \Big/ \left(3K_{\mathrm{n0}}^{i}\right), \mathrm{else} \end{cases} \tag{17}$$

The DSA theory postulates that in-situ stress is relieved, and hydrostatic pressure is exerted on the surface of the rock mass, thereby inducing a particular stress state as

$$[\sigma]_{\mathrm{DSA}} = \left[-P_0 + \sigma_{xx}^{\mathrm{I}}, -P_0 + \sigma_{yy}^{\mathrm{I}}, -P_0 + \sigma_{zz}^{\mathrm{I}}, \tau_{xy}^{\mathrm{I}}, \tau_{xz}^{\mathrm{I}}, \tau_{yz}^{\mathrm{I}}\right]^{\mathrm{T}} \tag{18}$$

where $[\sigma]_{\mathrm{DSA}}$ - the stress matrix of rock mass in DSA mode; σ_{ij}^{I} -

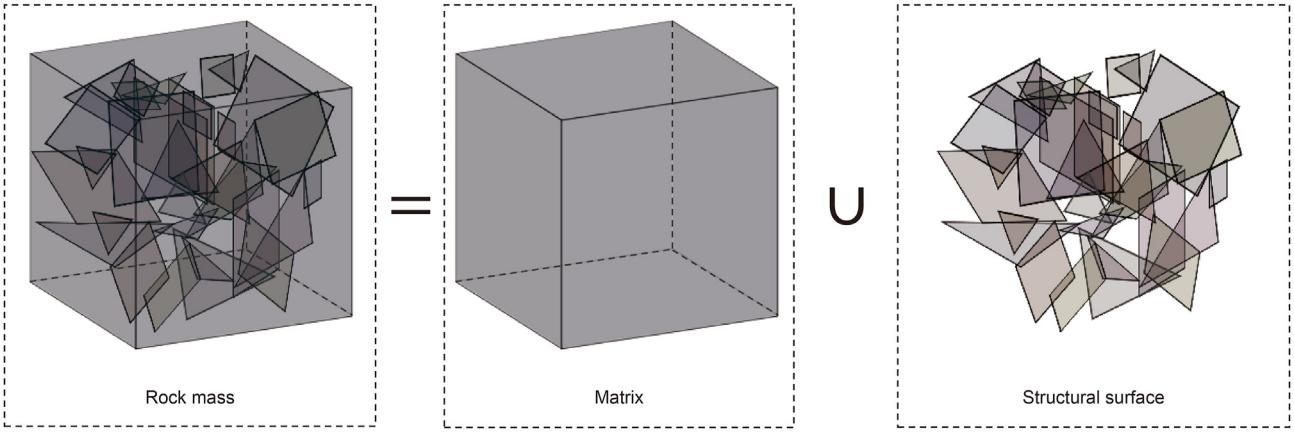

Fig. 9. The relationship between rock mass, matrix, and structural surfaces.

released in-situ stress components.

Project the $[\sigma]_{\mathrm{DSA}}$ to the $\boldsymbol{N}_3$, then σ_{n} is obtained as follows

$$\sigma_{\mathrm{n}}^{i} = -P_0 + C_i \tag{19}$$

where

$$C_i = \left(l_3^i\right)^2 \sigma_{xx}^{\mathrm{I}} + \left(m_3^i\right)^2 \sigma_{yy}^{\mathrm{I}} + \left(n_3^i\right)^2 \sigma_{zz}^{\mathrm{I}} + l_3^i m_3^i \tau_{xy}^{\mathrm{I}} + l_3^i n_3^i \tau_{xz}^{\mathrm{I}} + m_3^i n_3^i \tau_{yz}^{\mathrm{I}} \tag{20}$$

where: l_3^i, m_3^i, n_3^i - direction cosine of $\vec{N}_3^i$.

3.1.2. Micro-fractures tangential displacement

The fracture surfaces are rough. The shear strength of fractures conforms to the Mohr-Coulomb criterion as follows

$$\tau_{\mathrm{p}}^{i} = f_i \sigma_{\mathrm{n}}^{i} + c_i \tag{21}$$

where: τ_{p}^{i} - shear strength; f_i - friction coefficient; c_i - cohesion.

The shear stiffness model is proposed by Clough and Duncan (1978) as defined by the equation

$$K_{\mathrm{s}}^{i} = \begin{cases} K_{\mathrm{s0}}^{i}\left(1 - R_{\mathrm{c}}\tau_{\mathrm{s}}^{i}/\tau_{\mathrm{p}}^{i}\right), \tau_{\mathrm{s}}^{i} < \tau_{\mathrm{p}}^{i} \\ K_{\mathrm{s0}}^{i}(1 - R_{\mathrm{c}})^2, \text{else} \end{cases} \tag{22}$$

where: K_{s}^{i} – fracture shear strength; K_{s0}^{i} – initial fracture shear strength; τ_{s}^{i} – shear stress; R_{c} – a constant positive close to 1.

Similar to normal stress, the shear stress in DSA theory is derived

$$\tau_{\mathrm{s}}^{i} = \sqrt{\left(T_X^i\right)^2 + \left(T_Y^i\right)^2 + \left(T_Z^i\right)^2 - \left(\sigma_{\mathrm{n}}^{i}\right)^2} \tag{23}$$

where

$$\begin{cases} T_X^i = -l_3^i P_0 + \left(l_3^i \sigma_{xx} + \left(m_3^i \tau_{xy} + n_3^i \tau_{xz}\right)/2\right) = -l_3^i P_0 + D_X^i \\ T_Y^i = -m_3^i P_0 + \left(m_3^i \sigma_{yy} + \left(l_3^i \tau_{xy} + n_3^i \tau_{yz}\right)/2\right) = -m_3^i P_0 + D_Y^i \\ T_Z^i = -n_3^i P_0 + \left(n_3^i \sigma_{zz} + \left(l_3^i \tau_{xz} + m_3^i \tau_{yz}\right)/2\right) = -n_3^i P_0 + D_Z^i \end{cases} \tag{24}$$

Combining Eqs. (23) and (24), the shear stress is simplified as follows

$$\tau_{\mathrm{s}}^{i} = \left(D_X^i\right)^2 + \left(D_Y^i\right)^2 + \left(D_Z^i\right)^2 - C_i^2 \tag{25}$$

As shown in Eq. (25), in DSA mode, the shear stress is simplified to a constant. The relationship between δ_{s} and τ_{s} is given by the following equation

$$\mathrm{d}\delta_{\mathrm{s}}^{i} = \mathrm{d}\tau_{\mathrm{s}}^{i} / K_{\mathrm{s}}^{i} \tag{26}$$

Based on Eqs. (25) and (26), and noting that the shear displacement is zero in the initial state, the shear displacement of micro-fractures is always zero in the DSA loading mode.

3.1.3. Rock mass strain

Rock mass deformation is characterized by two distinct types of strain, namely matrix strain and micro-fracture displacement. In the local coordinate of micro-fracture, as shown in Fig. 11, the i-th fracture strain is obtained via fracture displacement as follows

$$\begin{cases} \varepsilon_{33}^{\mathrm{f}i} = \delta_{\mathrm{n}}^{i} S_i / V \\ \gamma_{23}^{\mathrm{f}i} = \gamma_{32}^{\mathrm{f}i} = \left(\delta_{\mathrm{s}}^{i} \cdot \boldsymbol{N}_2^i\right) S_i / (2V) \\ \gamma_{13}^{\mathrm{f}i} = \gamma_{31}^{\mathrm{f}i} = \left(\delta_{\mathrm{s}}^{i} \cdot \boldsymbol{N}_1^i\right) S_i / (2V) \\ \varepsilon_{11}^{\mathrm{f}i} = \varepsilon_{22}^{\mathrm{f}i} = \gamma_{12}^{\mathrm{f}i} = \gamma_{21}^{\mathrm{f}i} = 0 \end{cases} \tag{27}$$

where $\varepsilon_{ij}^{\mathrm{f}i}$ - the strain components of i-th fracture; S_i - the fracture surface area; V - the rock mass volume.

The default $\boldsymbol{N}_2^i$ is parallel to one of the fracture surface edges to simplify the problem. Then, the γ_{f}^{i} is equal to zero. Consequently, the direction cosine of the local coordinate system is shown as follows

$$\begin{cases} l_1^{\mathrm{f}i} = \cos\alpha_{\mathrm{f}}^{\mathrm{i}} \sin\beta_{\mathrm{f}}^{i} \\ m_1^{\mathrm{f}i} = \cos\alpha_{\mathrm{f}}^{\mathrm{i}} \sin\beta_{\mathrm{f}}^{i} \\ n_1^{\mathrm{f}i} = -\sin\alpha_{\mathrm{f}}^{\mathrm{i}} \\ l_2^{\mathrm{f}i} = -\cos\beta_{\mathrm{f}}^{i} \\ m_2^{\mathrm{f}i} = \sin\beta_{\mathrm{f}}^{i} \\ n_2^{\mathrm{f}i} = 0 \\ l_3^{\mathrm{f}i} = \sin\alpha_{\mathrm{f}}^{\mathrm{i}} \sin\beta_{\mathrm{f}}^{i} \\ m_3^{\mathrm{f}i} = \sin\alpha_{\mathrm{f}}^{\mathrm{i}} \cos\beta_{\mathrm{f}}^{i} \\ n_3^{\mathrm{f}i} = \cos\alpha_{\mathrm{f}}^{\mathrm{i}} \end{cases} \tag{28}$$

where: $\alpha_{\mathrm{f}}^{\mathrm{i}}$, $\beta_{\mathrm{f}}^{\mathrm{i}}$, $\gamma_{\mathrm{f}}^{\mathrm{i}}$ - the i-th fracture's dip angles.

Thus, in the global coordinate system, the micro-fractures strain can be calculated using the following equations

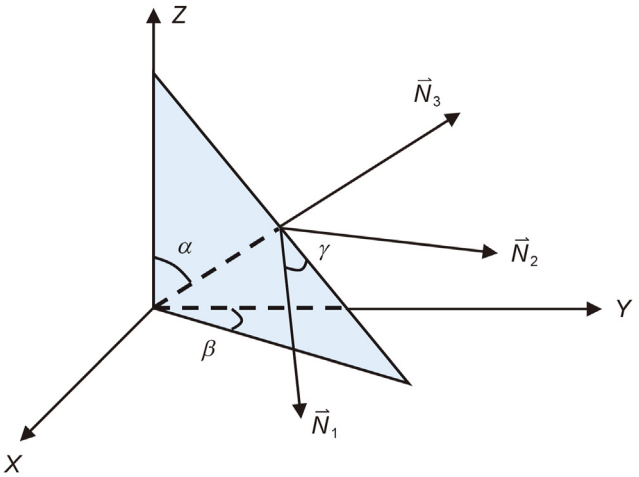

Fig. 11. Schematic diagram of the relationship between the local and global coordinate systems. α, β, γ are angles between the coordinate systems, whose domains are [0, π/2].

$$\begin{cases} \varepsilon_{xx}^{fi} = l_1^{fi} l_3^{fi} \gamma_{13}^{fi} + l_2^{fi} l_3^{fi} \gamma_{23}^{fi} + \left(l_3^{fi}\right)^2 \varepsilon_{33}^{fi} \\ \varepsilon_{yy}^{fi} = m_1^{fi} m_3^{fi} \gamma_{13}^{fi} + m_2^{fi} m_3^{fi} \gamma_{23}^{fi} + \left(m_3^{fi}\right)^2 \varepsilon_{33}^{fi} \\ \varepsilon_{zz}^{fi} = n_1^{fi} n_3^{fi} \gamma_{13}^{fi} + n_2^{fi} n_3^{fi} \gamma_{23}^{fi} + \left(n_3^{fi}\right)^2 \varepsilon_{33}^{fi} \\ \gamma_{xy}^{fi} = \gamma_{yx}^{fi} = \left(\left(l_1^{fi} m_3^{fi} + l_3^{fi} m_1^{fi}\right)\gamma_{13}^{fi} + \left(l_2^{fi} m_3^{fi} + l_3^{fi} m_2^{fi}\right)\gamma_{23}^{fi}\right)/2 + l_3^{fi} m_3^{fi} \varepsilon_{33}^{fi} \\ \gamma_{xz}^{fi} = \gamma_{zx}^{fi} = \left(\left(n_1^{fi} m_3^{fi} + n_3^{fi} m_1^{fi}\right)\gamma_{13}^{fi} + \left(n_2^{fi} m_3^{fi} + n_3^{fi} m_2^{fi}\right)\gamma_{23}^{fi}\right)/2 + n_3^{fi} m_3^{fi} \varepsilon_{33}^{fi} \\ \gamma_{yz}^{fi} = \gamma_{zy}^{fi} = \left(\left(n_1^{fi} l_3^{fi} + n_3^{fi} l_1^{fi}\right)\gamma_{13}^{fi} + \left(n_2^{fi} l_3^{fi} + n_3^{fi} l_2^{fi}\right)\gamma_{23}^{fi}\right)/2 + n_3^{fi} l_3^{fi} \varepsilon_{33}^{fi} \end{cases} \tag{29}$$

The rock mass's strain is derived as follows

$$[\varepsilon]_{\mathrm{DSA}} = \begin{bmatrix} \varepsilon_{xx}^{\mathrm{DSA}} \\ \varepsilon_{yy}^{\mathrm{DSA}} \\ \varepsilon_{zz}^{\mathrm{DSA}} \\ \gamma_{xy}^{\mathrm{DSA}} \\ \gamma_{xz}^{\mathrm{DSA}} \\ \gamma_{yz}^{\mathrm{DSA}} \end{bmatrix} = \begin{bmatrix} \varepsilon_{xx}^{\mathrm{m}} + \sum_{i=1}^{N_\mathrm{f}} \varepsilon_{xx}^{fi} \\ \varepsilon_{yy}^{\mathrm{m}} + \sum_{i=1}^{N_\mathrm{f}} \varepsilon_{yy}^{fi} \\ \varepsilon_{zz}^{\mathrm{m}} + \sum_{i=1}^{N_\mathrm{f}} \varepsilon_{zz}^{fi} \\ \gamma_{xy}^{\mathrm{m}} + \sum_{i=1}^{N_\mathrm{f}} \gamma_{xy}^{fi} \\ \gamma_{xz}^{\mathrm{m}} + \sum_{i=1}^{N_\mathrm{f}} \gamma_{xz}^{fi} \\ \gamma_{yz}^{\mathrm{m}} + \sum_{i=1}^{N_\mathrm{f}} \gamma_{yz}^{fi} \end{bmatrix} = \begin{bmatrix} \left(-P_0 + \sigma_{xx}^{\mathrm{I}}\right)(1-2\upsilon)/E + \sum_{i=1}^{N_\mathrm{f}} \varepsilon_{xx}^{fi} \\ \left(-P_0 + \sigma_{yy}^{\mathrm{I}}\right)(1-2\upsilon)/E + \sum_{i=1}^{N_\mathrm{f}} \varepsilon_{yy}^{fi} \\ \left(-P_0 + \sigma_{zz}^{\mathrm{I}}\right)(1-2\upsilon)/E + \sum_{i=1}^{N_\mathrm{f}} \varepsilon_{zz}^{fi} \\ \tau_{xy}^{\mathrm{I}}/G + \sum_{i=1}^{N_\mathrm{f}} \gamma_{xy}^{fi} \\ \tau_{xz}^{\mathrm{I}}/G + \sum_{i=1}^{N_\mathrm{f}} \gamma_{xz}^{fi} \\ \tau_{yz}^{\mathrm{I}}/G + \sum_{i=1}^{N_\mathrm{f}} \gamma_{yz}^{fi} \end{bmatrix} \tag{30}$$

where: N_f - the number of micro-fractures; G - the shear modulus of the matrix.

3.2. Verification results

The DSA and IDSA theories apply hydrostatic pressure to the rock mass surface. IDSA theory assumes hydrostatic pressure does not affect measurement results when the principal elastic axis is perpendicular to the rock surface. In-situ stress is parallel to the principal elastic axis, making the loading direction of hydrostatic pressure parallel to the direction of in-situ stress. Shear stresses on the rock mass surface are zero. Parameters from Table 2 are used to simulate the rock mass unit.

K_n^i and σ_{nmax}^i are randomly generated within the range of values.

Table 2
Input parameters of the numerical rock mass model.

Parameters	Values	Parameters	Values
E, GPa	40	K_n^i, MPa	13.5–16.5
υ	0.24	σ_{nmax}^i, MPa	11~33
L, mm	50	$\sigma_\mathrm{H}^\mathrm{I}$, MPa	25
N_f	50	$\sigma_\mathrm{h}^\mathrm{I}$, MPa	20
Fractures' total area, mm^2	100	$\sigma_\mathrm{v}^\mathrm{I}$, MPa	27

The area of the fracture is obtained by randomly allocating the fractures' total area. Then, the simulated DSA experiment is carried out, as shown in Fig. 12.

As the analytical model cannot emulate the IPM process, the initial elastic parameters of the simulated rock mass are employed as input values to determine in-situ stress. The slope of each strain curve's tangent at the origin in Fig. 12(a) is first computed. Subsequently, the constitutive equation is employed to derive the elastic parameter equation, represented by Eq. (31).

$$\begin{bmatrix} \mathrm{d}\varepsilon_{xx}^{\mathrm{DSA}} \\ \mathrm{d}\varepsilon_{yy}^{\mathrm{DSA}} \\ \mathrm{d}\varepsilon_{zz}^{\mathrm{DSA}} \\ \mathrm{d}\gamma_{xy}^{\mathrm{DSA}} \\ \mathrm{d}\gamma_{xz}^{\mathrm{DSA}} \\ \mathrm{d}\gamma_{yz}^{\mathrm{DSA}} \end{bmatrix} = \begin{bmatrix} S_{11} & S_{12} & S_{13} & S_{14} & S_{15} & S_{16} \\ S_{21} & S_{22} & S_{23} & S_{24} & S_{25} & S_{26} \\ S_{31} & S_{32} & S_{33} & S_{34} & S_{35} & S_{36} \\ S_{41} & S_{42} & S_{43} & S_{44} & S_{45} & S_{46} \\ S_{51} & S_{52} & S_{53} & S_{54} & S_{55} & S_{56} \\ S_{61} & S_{62} & S_{63} & S_{64} & S_{65} & S_{66} \end{bmatrix}_{xyz} \begin{bmatrix} \mathrm{d}P_0 \\ \mathrm{d}P_0 \\ \mathrm{d}P_0 \\ 0 \\ 0 \\ 0 \end{bmatrix} \tag{31}$$

where

$$[S]_{xyz} = [T]^{\mathrm{T}} [S]_{123} [T] \tag{32}$$

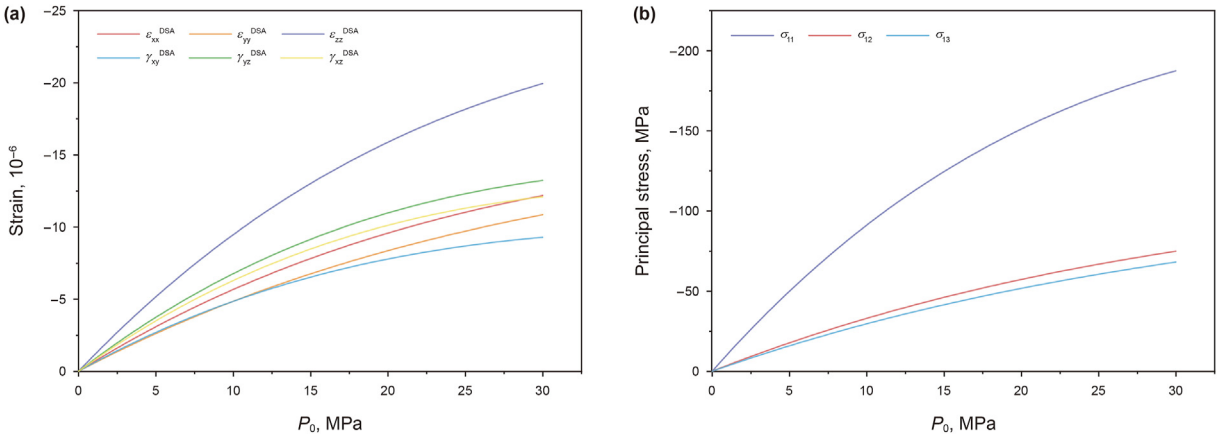

Fig. 12. Simulated DSA experiment results: (**a**) strain curves; (**b**) principal stress curves.

$$[T]=\begin{bmatrix} (l_1^{\mathrm{m}})^2 & (l_2^{\mathrm{m}})^2 & (l_3^{\mathrm{m}})^2 & 2l_1^{\mathrm{m}}l_2^{\mathrm{m}} & 2l_1^{\mathrm{m}}l_3^{\mathrm{m}} & 2l_1^{\mathrm{m}}l_3^{\mathrm{m}} \\ (m_1^{\mathrm{m}})^2 & (m_2^{\mathrm{m}})^2 & (m_3^{\mathrm{m}})^2 & 2m_1^{\mathrm{m}}m_2^{\mathrm{m}} & 2m_1^{\mathrm{m}}m_3^{\mathrm{m}} & 2m_2^{\mathrm{m}}m_3^{\mathrm{m}} \\ (n_1^{\mathrm{m}})^2 & (n_2^{\mathrm{m}})^2 & (n_3^{\mathrm{m}})^2 & 2n_1^{\mathrm{m}}n_2^{\mathrm{m}} & 2n_1^{\mathrm{m}}n_3^{\mathrm{m}} & 2n_2^{\mathrm{m}}n_3^{\mathrm{m}} \\ l_1^{\mathrm{m}}m_1^{\mathrm{m}} & l_2^{\mathrm{m}}m_2^{\mathrm{m}} & l_3^{\mathrm{m}}m_3^{\mathrm{m}} & l_2^{\mathrm{m}}m_1^{\mathrm{m}}+l_1^{\mathrm{m}}m_2^{\mathrm{m}} & l_3^{\mathrm{m}}m_1^{\mathrm{m}}+l_1^{\mathrm{m}}m_3^{\mathrm{m}} & l_2^{\mathrm{m}}m_3^{\mathrm{m}}+l_3^{\mathrm{m}}m_2^{\mathrm{m}} \\ l_1^{\mathrm{m}}n_1^{\mathrm{m}} & l_2^{\mathrm{m}}n_2^{\mathrm{m}} & l_3^{\mathrm{m}}n_3^{\mathrm{m}} & l_2^{\mathrm{m}}n_1^{\mathrm{m}}+l_1^{\mathrm{m}}n_2^{\mathrm{m}} & l_3^{\mathrm{m}}n_1^{\mathrm{m}}+l_1^{\mathrm{m}}n_3^{\mathrm{m}} & l_2^{\mathrm{m}}n_3^{\mathrm{m}}+l_3^{\mathrm{m}}n_2^{\mathrm{m}} \\ m_1^{\mathrm{m}}n_1^{\mathrm{m}} & m_2^{\mathrm{m}}n_2^{\mathrm{m}} & m_3^{\mathrm{m}}n_3^{\mathrm{m}} & m_2^{\mathrm{m}}n_1^{\mathrm{m}}+m_1^{\mathrm{m}}n_2^{\mathrm{m}} & m_3^{\mathrm{m}}n_1^{\mathrm{m}}+m_1^{\mathrm{m}}n_3^{\mathrm{m}} & m_2^{\mathrm{m}}n_3^{\mathrm{m}}+m_3^{\mathrm{m}}n_2^{\mathrm{m}} \end{bmatrix} \tag{33}$$

$$\begin{cases} l_1^{\mathrm{m}}=\cos\alpha_{\mathrm{m}}\sin\beta_{\mathrm{m}}\cos\gamma_{\mathrm{m}}+\cos\beta_{\mathrm{m}}\sin\gamma_{\mathrm{m}} \\ m_1^{\mathrm{m}}=\cos\alpha_{\mathrm{m}}\cos\beta_{\mathrm{m}}\cos\gamma_{\mathrm{m}}-\sin\beta_{\mathrm{m}}\sin\gamma_{\mathrm{m}} \\ n_1^{\mathrm{m}}=-\sin\alpha_{\mathrm{m}}\cos\gamma_{\mathrm{m}} \\ l_2^{\mathrm{m}}=\cos\alpha_{\mathrm{m}}\sin\beta_{\mathrm{m}}\sin\gamma_{\mathrm{m}}-\cos\beta_{\mathrm{m}}\cos\gamma_{\mathrm{m}} \\ m_2^{\mathrm{m}}=\cos\alpha_{\mathrm{m}}\cos\beta_{\mathrm{m}}\sin\gamma_{\mathrm{m}}+\sin\beta_{\mathrm{m}}\cos\gamma_{\mathrm{m}} \\ n_2^{\mathrm{m}}=-\sin\alpha_{\mathrm{m}}\sin\gamma_{\mathrm{m}} \\ l_3^{\mathrm{m}}=\sin\alpha_{\mathrm{m}}\sin\beta_{\mathrm{m}} \\ m_3^{\mathrm{m}}=\sin\alpha_{\mathrm{m}}\cos\beta_{\mathrm{m}} \\ n_3^{\mathrm{m}}=\cos\alpha_{\mathrm{m}} \end{cases} \tag{34}$$

where: α_{m}, β_{m}, γ_{m} - the angles between the principal elastic axis and global coordinates. And,

$$[S]_{123}=\begin{bmatrix} 1/E_1 & -\upsilon_{12}/E_1 & -\upsilon_{13}/E_1 & 0 & 0 & 0 \\ -\upsilon_{12}/E_1 & 1/E_2 & -\upsilon_{23}/E_2 & 0 & 0 & 0 \\ -\upsilon_{13}/E_1 & -\upsilon_{23}/E_2 & 1/E_3 & 0 & 0 & 0 \\ 0 & 0 & 0 & 1/G_{12} & 0 & 0 \\ 0 & 0 & 0 & 0 & 1/G_{13} & 0 \\ 0 & 0 & 0 & 0 & 0 & 1/G_{23} \end{bmatrix} \tag{35}$$

The orthotropic elastic parameters are acquired using the method presented in Chapter 4. The fitness value is assessed by calculating the sum of absolute values of the relative errors between the values obtained from Eq. (31) and the actual values. Table 3 displays the range and inversion outcomes of orthotropic elastic parameters. Additionally, Fig. 13 portrays the fitness iteration curve.

Table 3
Inversion results of numerical rock mass model orthotropic parameters.

Parameters	Ranges	Results
E_x, GPa	0.5–50	0.6449
E_y, GPa	0.5–50	1.5702
E_z, GPa	0.5–50	1.3328
υ_{xy}	0.001–0.51	0.5096
υ_{xz}	0.001–0.51	0.5098
υ_{yz}	0.001–0.51	0.0099
G_{xy}, GPa	1~50	32.348
G_{xz}, GPa	1~50	34.382
G_{yz}, GPa	1~50	40.306
α,°	0~90	0.9191
β,°	0~90	0.2615
γ,°	0~90	0.3455

The simulated rock mass is fictional; thus, the inverted elastic parameters may deviate from the actual ones. Additionally, microfractures result in the significant softness of the rock mass and could even lead to abnormal expansion during compression (Wong et al., 2008).

Then, the elastic parameters, as shown in Tables 2 and 3, are substituted into Eq. (14) to derive the in-situ stress based on the IDSA method. Finally, the in-situ stress was calculated based on the simulated DSA and IDSA tests, as shown in Table 4. The rock mass's virtue and the fractures' generalized randomness preclude a direct correlation between in-situ stress and fracture direction. Therefore,

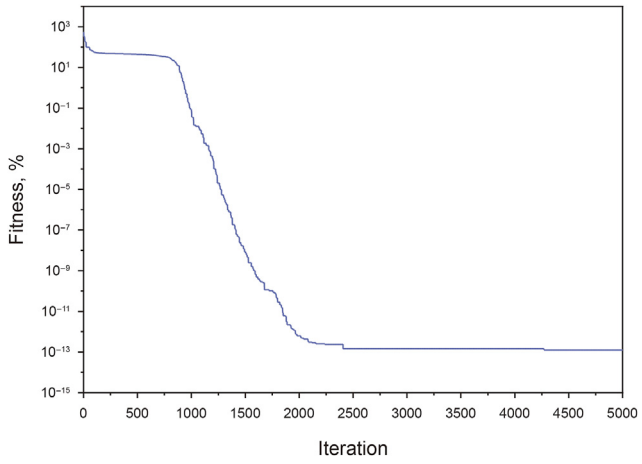

Fig. 13. Fitness curve of orthotropic parameters.

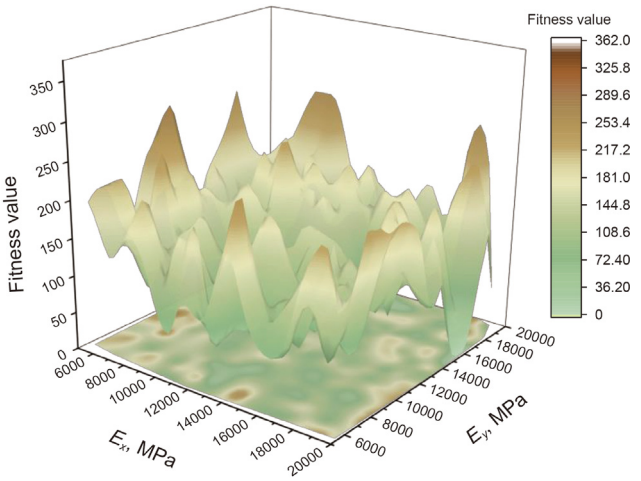

Fig. 15. Fitness function of elastic parameters inversion problem.

Table 4
In-situ stress inversion results.

	Actual values	Inversion results		Absolute relative errors, %	
		DSA	IDSA	DSA	IDSA
σ_{11}/σ_{33}	1.350	3.184	1.758	135.8	30.22
σ_{22}/σ_{33}	1.250	1.120	1.111	10.38	11.12
$\langle \sigma_{22}, \sigma_H^1 \rangle$,°	0	84.52	39.82	/	/
$\langle \sigma_{33}, \sigma_h^1 \rangle$,°	0	46.15	61.66	/	/
$\langle \sigma_{11}, \sigma_v^1 \rangle$,°	0	77.85	74.38	/	/

a significant miscalculation in stress direction occurs. The inversion results preliminarily verified the applicability of IDSA.

4. Algorithm for elastic parameters inversion

The inversion of elastic parameters is crucial for measuring in-situ stress. The sensing casing records varying strains for rock masses with different elastic parameters. Many strain measurement results can be obtained through the fiber optic on the casing. An optimization algorithm repeatedly iterates the elastic parameters until the error between numerical simulations and actual strain results meets allowable tolerance. By doing this, the elastic parameters are inverted.

4.1. Fitness function

The optimization algorithm's success hinges on an appropriate fitness function. A numerical simulation model is created by ABAQUS, as depicted in Fig. 14, with displacement constraints imposed on the cement sheath, casing, and rock mass surfaces. Pressure is applied inside the casing to replicate the IPM process. The shallow slots and fiber optic sensing casing structure are disregarded to simplify the model, assuming that fiber optic sensing only measures strain without affecting results. The strain conduction coefficient between the fiber optic and the casing is assumed to be 1. The numerical model is used to determine the strain of the sensing casing, which is then extracted and substituted into Eqs. (8) and (9) for fiber optic sensing simulation.

Specific rock mass elastic parameter (E_1, E_2, E_3, υ_{12}, υ_{13}, υ_{23}, G_{12}, G_{13}, G_{23}, α_m, β_m, γ_m) is taken as the actual value of the elastic parameter. The simulated fiber optic strain calculated under the elastic parameters is taken as the actual value of the strain. Hence, the fitness function is

$$w = \sum_{i=1}^{M} |A_i - F_i|/A_i \tag{36}$$

where: w - the fitness value; M - the number of sensing points; A_i and F_i are the actual and predicted value of the i-th sensing point.

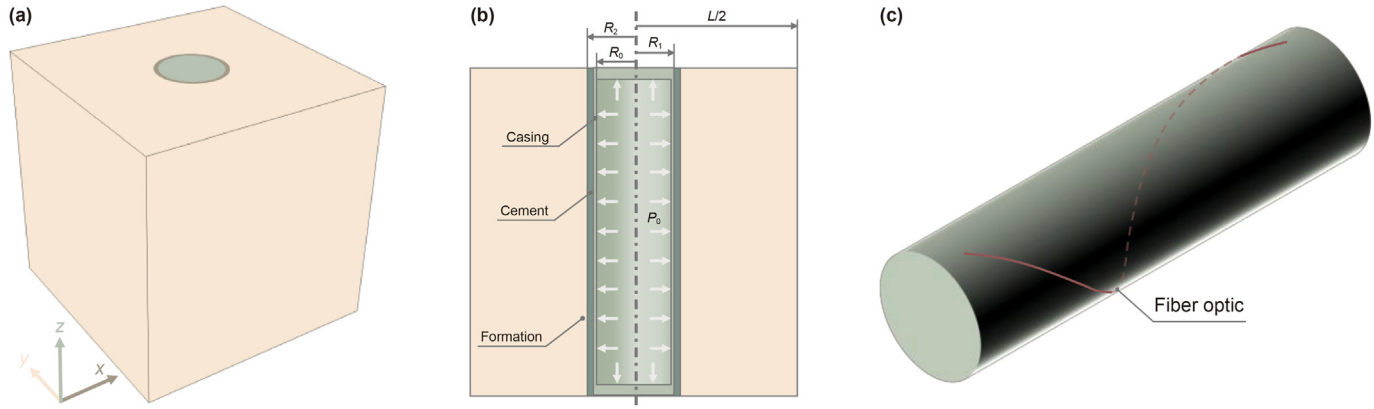

Fig. 14. Numerical simulation model: (**a**) the 3D view; (**b**) the cutaway view; (**c**) the structure of the sensing casing.

Fig. 15 illustrates that the fitness function is a challenging multimodal function, and optimizing such functions is difficult. During optimization, particles may become stuck in locally optimal solutions or prematurely. To overcome these issues, the Success-History based parameters Adaptation for Differential Evolution (SHADE) algorithm is a useful optimization technique. Compared to other algorithms, SHADE has proven effective in solving the abovementioned problems (Tanabe and Fukunaga, 2013).

4.2. O-SHADE algorithm

The O-SHADE algorithm uses differential evolution to invert rock mass orthotropic elastic parameters based on the SHADE algorithm, an improved version of the Differential Evolution (DE) algorithm. SHADE is a critical stochastic search method known for its robustness in dealing with multimodal problems. It is a typical greedy algorithm.

In the SHADE, the control parameters of the individuals that evolved successfully during the iteration are stored and randomly adopted to adjust the control parameters of the current iteration (Tanabe and Fukunaga, 2013).

The population of SHADE is represented as vectors consisting of a combination of parameters $X_i^t = (x_{1,i}^t,\ldots,x_{D,i}^t), i = 1,\ldots,N$, where D is dimensional of the problem, N is the population size, and t is iteration times. The iteration is initialized with a population generated randomly. The genes of initialized population individuals are limited between the maximum $MAX = (x_{1,\max},\ldots,x_{D,\max})$ and minimum $MIN = (x_{1,\min},\ldots,x_{D,\min})$ values of the corresponding loci. Each iteration is realized by mutation, crossover, and selection.

The current-to-*p*best/1 mutation strategy is adopted. The top $N \times p_i$ individuals with the lowest fitness value ranked as the elite in the t-th generation population (P_t) participating in the mutation operation. Besides, $p_i \in [2/N, 0.2]$, for each individual, is randomly generated.

The following equation gives the mutation strategy

$$V_i^t = X_i^t + F_i^t \cdot \left(X_{p\text{best}}^t - X_i^t\right) + F_i^t \cdot (X_{r1}^t - X_{r2}^t) \tag{37}$$

where, V_i^t is the i-th mutant individual in the t-th generation. The $X_{p\text{best}}^t$ is selected from elite individuals randomly. And the vectors X_{r1}^t and X_{r2}^t are different from each other and randomly selected from $P^t \cup A$, where A is the external archive stored part of failed individuals from the first to $(t-1)$-th generation. Besides, $F_i^t \in [0,1]$ is the scaling factor in the t-th generation.

The mutant vectors in the t-th generation are obtained via the mutation. Consequently, the genes of mutant vectors and the t-th individuals will be combined randomly

$$u_{j,i}^t = \begin{cases} v_{j,i}^t, \text{rand} < CR_i^t \text{ or } j = j_{\text{rand}} \\ x_{j,i}^t, \text{else} \end{cases} \tag{38}$$

In Eq. (38), $u_{j,i}^t$ is the j-th crossed gene of the i-th individual of the t-th generation. Besides, $v_{j,i}^t$ and $x_{j,i}^t$ are j-th mutated and original genes. $CR_i^t \in [0,1]$ is crossover rate. And $j_{\text{rand}} \in [1,D] \cap Z$ is a uniformly randomly generated integer.

In the iteration process, it is inevitable that $u_{j,i}^t$ exceeds the boundary value of the loci. The average method is adopted when problems occur. In other words, $u_{j,i}^t$ is assigned as the average of $u_{j,i}^t$ and the $x_{j,\min}$ when $u_{j,i}^t$ is less than the $x_{j,\min}$. Similarly, $u_{j,i}^t$ is assigned as the average of $u_{j,i}^t$ and the $x_{j,\max}$ when $u_{j,i}^t$ is greater than the $x_{j,\max}$.

Consequently, the selection procedure is going to be manipulated as follows

$$X_i^{t+1} = \begin{cases} U_i^t, f(U_i^t) < f(X_i^t) \\ X_i^t, \text{else} \end{cases} \tag{39}$$

where: X_i^t - original individuals; U_i^t - crossed individuals. Correspondingly, $f(X_i^t)$ and $f(U_i^t)$ are fitness values of X_i^t and U_i^t.

The evolved individuals' scaling factor and crossover rate are stored in S_F and S_{CR}. These archives have a capacity that is consistent with the population size N. When the number of stored information reaches the archives' capacity, new information will overwrite the first information.

The individual information will be saved in the external archive, A when an individual fails to evolve to the next generation. The capacity of A is consistent with N. Randomly delete an individual in A to make space for the new individual when the storage capacity in A reaches the upper limit.

In each generation, the scaling factor and crossover rate are updated randomly. The scaling factor follows the Cauchy distribution, and the crossover rate follows the normal distribution. The control parameters are selected by the index r_i, which is generated randomly from [1, N]. The distribution function acted as follows

$$F_i^t = \text{randc}_i(M_{F,r_i}, 0.1) \tag{40}$$

$$CR_i^t = \text{randn}_i(M_{CR,r_i}, 0.1) \tag{41}$$

CR_i^t will be forcibly assigned to the adjacent endpoint when it exceeds the domain. Similarly, F_i^t is forced to be one when it exceeds the upper limit of the domain. In contrast, it will be randomly generated again until its value is not less than the lower limit of the domain when it is lower than the lower limit of the domain. In Eq. (40), M_{F,r_i} is a controlling factor and is

$$M_{F,r_i}^{t+1} = \begin{cases} \text{mean}_{WL}(S_F), S_F \neq \varnothing \\ 0.5, \quad t = 0 \\ M_{F,r_i}^t, \quad \text{else} \end{cases} \tag{42}$$

where

$$\text{mean}_{WL}(S_F) = \sum_{k=1}^{|S_F|} w_k \cdot S_{F,k}^2 \Big/ \left(\sum_{k=1}^{|S_F|} w_k \cdot S_{F,k}\right) \tag{43}$$

where: $|S_F|$ - the size of S_F; w_k - an individual's weight. And

$$w_k = \Delta f_k \Big/ \sum_{k=1}^{|S_F|} \Delta f_k \tag{44}$$

where $\Delta f_k = \left|f(u_k^t) - f(x_k^t)\right|$.

Similarly, in Eq. (41), M_{CR,r_i} is also a controlling factor and is calculated as follows

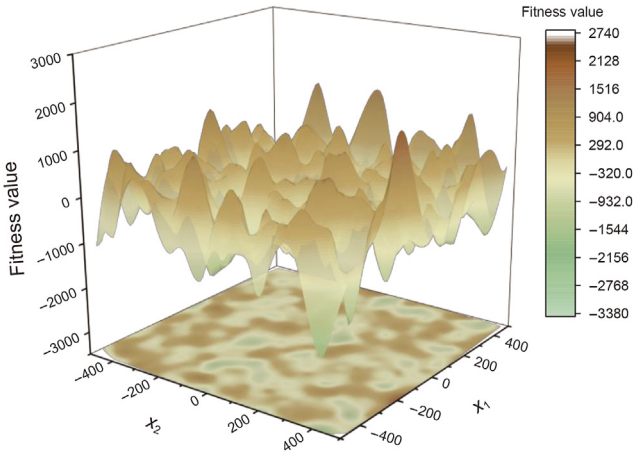

Fig. 16. GSP fitness value function map.

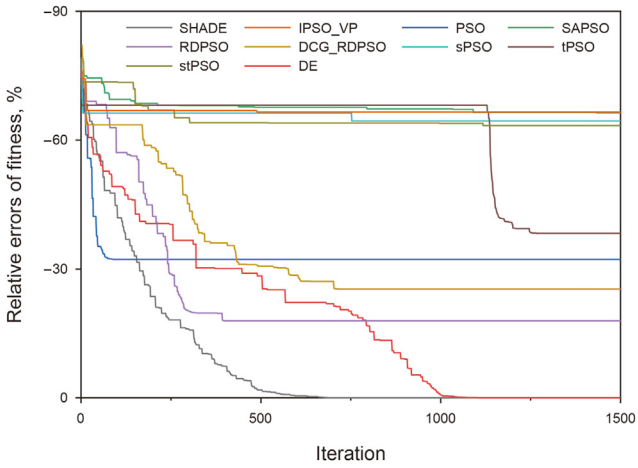

Fig. 17. Metaheuristic algorithms optimization results. The smaller the relative errors of fitness, the higher the inversion accuracy. When the relative fitness errors are close, the earlier the convergence is achieved, the better.

$$M_{CR,r_i}^{t+1} = \begin{cases} \text{mean}_{WA}(S_{CR}), S_{CR} \neq \varnothing \\ 0.5, \qquad t = 0 \\ M_{CR,r_i}^{t}, \qquad \text{else} \end{cases} \tag{45}$$

where

$$\text{mean}_{WA}(S_{CR}) = \sum_{k=1}^{|S_{CR}|} w_k \cdot S_{CR,k} \tag{46}$$

The preceding information outlines the fundamental tenets of the SHADE algorithm, which are applicable for unconstrained parameter optimization. However, the problem of inverting orthotropic elastic parameters constitutes a constrained optimization task with specific constraints. The constraints are as follows.

$$\begin{cases} E_1, E_2, E_3, G_{12}, G_{13}, G_{233} > 0 \\ |\upsilon_{12}| < \sqrt{E_1/E_2} \\ |\upsilon_{13}| < \sqrt{E_1/E_3} \\ |\upsilon_{23}| < \sqrt{E_2/E_3} \\ 1 - \upsilon_{12}\upsilon_{21} - \upsilon_{13}\upsilon_{31} - \upsilon_{23}\upsilon_{32} - 2\upsilon_{21}\upsilon_{32}\upsilon_{13} > 0 \end{cases} \tag{47}$$

O-SHADE regenerates individuals until they meet the inequality

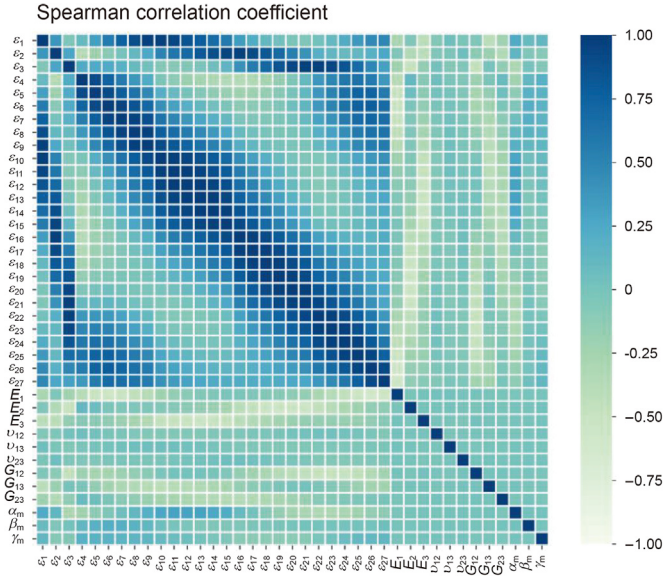

Fig. 18. Spearman correlation coefficient. $\varepsilon_1 \sim \varepsilon_{27}$ represent sensing points strain. The closer the correlation coefficient is to 1, the higher the positive correlation is. The closer the correlation coefficient is to −1, the higher the negative correlation is. The closer the correlation coefficient is to 0, the worse the correlation is.

Table 5
Parameters related to the metaheuristic algorithms.

Algorithm	Years	Parameters informations
PSO (Kennedy and Eberhart, 1995)	1995	$\omega = 0.99\text{^t}$, $c_1 = c_2 = 2$, $N = 150$.
DE (Rainer and Kenneth, 1997)	1997	$\beta_{\min} = 0.2$, $\beta_{\max} = 0.2$, p_{CR}=0.2, $N = 150$.
SAPSO (Wang and Li, 2004)	2004	$\omega = 0.99\text{^t}$, $c_1 = c_2 = 2$, $\lambda = 0.5$, $N = 150$.
sPSO (Hu and Li, 2007)	2007	$\omega = 0.99\text{^t}$, $c_1 = c_2 = 2$, $N = 150$.
tPSO (Hu and Li, 2007)	2007	$\omega = 0.99\text{^t}$, $c_1 = c_2 = 2$, $N = 150$.
stPSO (Hu and Li, 2007)	2007	$\omega = 0.99\text{^t}$, $c_1 = c_2 = 2$, $N = 150$.
SHADE (Tanabe and Fukunaga, 2013)	2013	$N = 150$, and the parameters mentioned in this study
RDPSO (Sun et al., 2013)	2013	α= 0.9−0.6 * t/MaxIt, β=1.45, $c_1 = c_2 = 2$, $N = 150$.
DCG_RDPSO (Chao, 2021)	2021	α_0=0.9, β=1.45, $c_1 = c_2 = 2$, c=7,er=1e-4.
IPSO-VP (Li and Gao, 2022)	2022	$\omega_{\max}$=0.9, $\omega_{\max}$=0.4, $c_1 = c_2 = 2$, δ=0.8.

conditions of Eq. (47). ABAQUS executes the numerical simulation process, which has a high calculation cost. Optimization problems require many iterative operations, increasing the calculation time. Hence, parallel computing technology is necessary to improve efficiency and reduce the calculation time.

The genes of individuals are transferred to INP files during the creation of the population U^t. Batches of numerical simulation jobs are established, submitted to ABAQUS, and computed in parallel. The computation results are extracted and calculated through scripts. Finally, fitness values are submitted to the SHADE algorithm.

4.3. Flow of O-SHADE

The O-SHADE algorithm, tailored for the IDSA approach, integrates SHADE and ABAQUS via parallel computation and joint simulation, resulting in increased computational efficacy. Moreover, it complements the limitations of orthotropic elastic parameters. Algorithm 1 provides a concise overview of the O-SHADE's workflow.

Algorithm 1. O-SHADE

// Initialization
$t = 0$;
Generate population $P^0 = (E_1^0, E_2^0, E_3^0, \upsilon_{12}^0, \upsilon_{13}^0, \upsilon_{23}^0, G_{12}^0, G_{13}^0, G_{23}^0, \alpha_{\mathrm{m}}^0, \beta_{\mathrm{m}}^0, \gamma_{\mathrm{m}}^0)$ randomly;
Initialize the values of M_{CR} and M_F to 0.5;
Establish $A = [\,]$;
$k = 1$;
// Main Loop
while $w >=$ Tol && $t <=$ MaxIt
  $S_{CR} = [\,]$, $S_F = [\,]$;
  for $i = 1 : N$
    while U_i^t **dose not meet the constraints**
      r_i = Select from $[1, N]$ randomly;
      $F_i^t = \mathrm{randc}_i(M_{F,r_i}, 0.1)$;
      $CR_i^t = \mathrm{randn}_i(M_{CR,r_i}, 0.1)$;
      $p_i = \mathrm{rand}(2/N, 0.2)$;
      Generate trial vector U_i^t by current-to-$p$best/1/bin;
    end
  end
  // Parallel Computing in ABAQUS
  Change the INP files in batches;
  Submit INP files to ABAQUS in batches;
  Extract the numerical simulation results in batches;
  Calculate the fitness values in batches;
  for $i = 1 : N$
    if $f(U_i^t) < f(X_i^t)$
      $X_i^{t+1} = U_i^t$;
    else
      $X_i^{t+1} = X_i^t$;
    end
    if $f(U_i^t) < f(X_i^t)$
      $X_i^t \rightarrow A$;
      $F_i^t \rightarrow S_F, CR_i^t \rightarrow S_{CR}$
    end
  end
  while size(A) > N
    Delete an individual stored in A randomly;
  end
  if isempty(S_{CR}) && isempty(S_F) ~= 0
    Update M_{F,r_i}^{t+1} and M_{CR,r_i}^{t+1};
    k ++;
    if $k > N$
      $k = 1$;
    end
  end
end

Table 6
Parameters related to the ML algorithms.

Algorithms	Years	Parameters
RT (Morgan and Sonquist, 1963)	1963	max_depth = 30, min_samples_leaf = 1, min_samples_split = 5
GBDT (Friedman, 2001)	2001	learning_rate = 0.01, max_depth = 15, n_estimators = 2000
XGBoost (Chen et al., 2015)	2014	learning_rate = 0.01, max_depth = 20, n_estimators = 1000

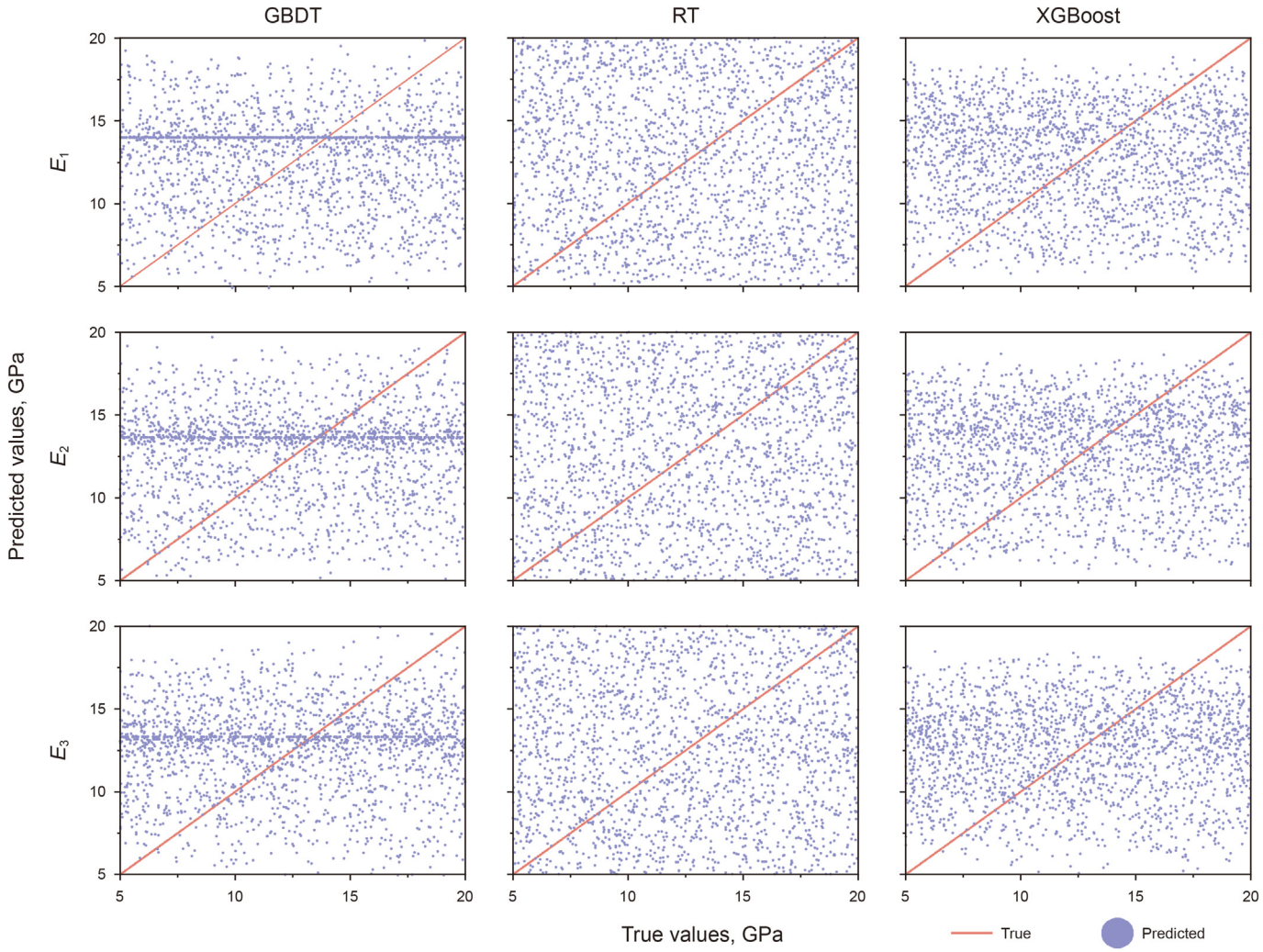

Fig. 19. Prediction results of the ML algorithms.

Table 7
Inversion results of numerical rock mass model orthotropic parameters.

	MAPEs, %			Absolut relative errors, %
	GBDT	RT	XGBoost	O-SHADE
E_1, GPa	23.55	29.38	22.21	0.006667
E_2, GPa	25.12	32.15	24.64	0.008333
E_3, GPa	24.81	31.57	23.73	0.068889
υ_{12}	18.09	22.94	17.80	0.208330
υ_{13}	18.31	23.23	18.22	0.115380
υ_{23}	18.00	22.93	17.95	0.096774
G_{12}, GPa	22.97	29.32	22.24	0.022222
G_{13}, GPa	24.75	31.35	24.11	0.048571
G_{23}, GPa	23.70	30.54	22.76	0.000000
α_m,°	234.9	179.5	192.0	0.020000
β_m,°	222.8	3.000	211.5	0.040000
γ_m,°	465.7	518.5	504.5	0.028571

Table 8
Inversion results of numerical rock mass model orthotropic parameters.

Parameters	Values	Parameters	Values
E_c, GPa	206	R_0, mm	34.5
υ_c	0.304	R_1, mm	37.5
E_s, GPa	5	R_2, mm	42.5
υ_s	0.24	L, mm	300
P_0, MPa	20	M	27
φ,°	49.2	Tol	0.002

4.4. Comparative analysis of the algorithms

4.4.1. Comparison between metaheuristic algorithms

The optimization algorithm known as the metaheuristic algorithm includes SHADE among its methods. Selecting the

Table 9
Actual value and range of orthotropic elastic parameters (Gui et al., 2019; Li et al., 2011).

Parameters	Actual values		Ranges	
	Sandstone	Shale	Sandstone	Shale
E_1, GPa	15	19	5~20	15~30
E_2, GPa	12	22	5~20	15~30
E_3, GPa	9	26	5~20	15~30
υ_{12}	0.24	0.26	0.2–0.4	0.2–0.4
υ_{13}	0.26	0.30	0.2–0.4	0.2–0.4
υ_{23}	0.31	0.32	0.2–0.4	0.2–0.4
G_{12}, GPa	9	8	5~15	5~15
G_{13}, GPa	7	10	5~15	5~15
G_{23}, GPa	10	11	5~15	5~15
α_m,°	30	30	0~90	0~90
β_m,°	45	45	0~90	0~90
γ_m,°	70	70	0~90	0~90

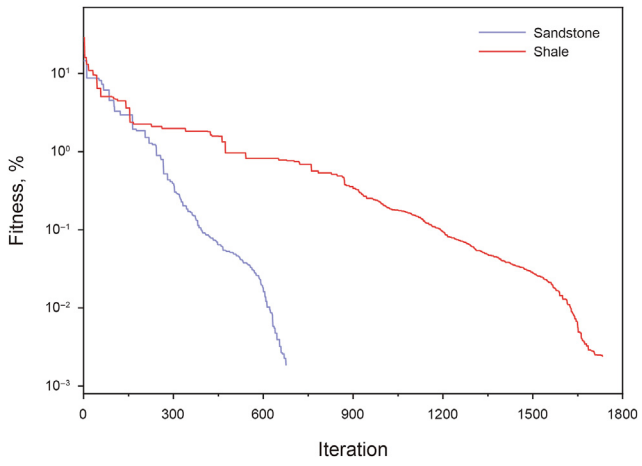

Fig. 20. Convergence curves of O-SHADE.

Table 10
Inversion results of orthotropic elastic parameters.

Parameters	Actual values		Inversion values		Absolut relative errors, %	
	Sandstone	Shale	Sandstone	Shale	Sandstone	Shale
E_1, GPa	15	19	15.001	19.013	0.006667	0.068421
E_2, GPa	12	22	11.999	22.027	0.008333	0.12273
E_3, GPa	9	26	9.0062	25.934	6.008889	0.25385
υ_{12}	0.24	0.26	0.2405	0.2601	0.20833	0.038462
υ_{13}	0.26	0.30	0.2597	0.2998	0.11538	0.066667
υ_{23}	0.31	0.32	0.3097	0.3205	0.096774	0.15625
G_{12}, GPa	9	8	9.0020	7.9961	0.022222	0.048750
G_{13}, GPa	7	10	6.9966	10.001	0.048571	0.010000
G_{23}, GPa	10	11	10.000	11.014	0.000000	0.12727
α_m,°	30	30	30.006	29.964	0.020000	0.12000
β_m,°	45	45	45.018	45.097	0.040000	0.21556
γ_m,°	70	70	69.980	69.922	0.028571	0.11143

appropriate test function is critical for selecting the optimal algorithm. However, the optimization algorithm entails numerous iterations, resulting in substantial computing expenses. Therefore, using a complex multimodal function instead of the inversion problem is preferable to enhance selection efficiency.

For this purpose, the Generalized Schwefel's Problem (GSP) is taken as the test function. GSP's fitness value is demonstrated in Eq. (48) and Fig. 16. Like the elastic parameters inversion problem, GSP is a typical multimodal problem. If the algorithm underperforms in GSP, it will perform similarly poorly in the elastic parameters inversion.

$$w_s = -\sum_{i=1}^{30} x_i \sin\left(\sqrt{|x_i|}\right), -500 \le x_i \le 500 \tag{48}$$

where: w_s - the fitness value of GSP. And, $\min(w_s) = w_s(420.9687, \ldots, 420.9687) = -12569.5$.

Some of the metaheuristic algorithms are selected to be compared with SHADE. The algorithms are listed in Table 5. As shown in Fig. 17, the SHADE shows tremendous advantages.

4.4.2. Comparison with machine learning algorithms

Machine learning (ML) algorithms have performed well in parameter prediction and inversion and have been widely used (Fan et al., 2022). In particular, Gradient Boosted Decision Tree (GBDT), Regression Tree (RT), and XGBoost algorithms are often used for the nonlinear inversion of parameters (Alabdullah et al., 2022; Alnahit et al., 2022; Weng and Paal, 2022). The computing cost of ML algorithms is much lower than metaheuristic algorithms. Therefore, the comparative analysis directly tests the orthotropic elastic parameter inversion problem.

Unlike O-SHADE, in the ML algorithms, the fiber optic strain is substituted into the trained prediction model to invert elastic parameters. Based on the related parameters in Table 9 and the parameters range of sandstone in Table 8, a data set with a size of 10,000 was randomly generated. As shown in Fig. 18, the Spearman correlation coefficient is analyzed. It can be seen that the correlation between strain and elastic parameters is poor.

The parameters of ML algorithms are shown in Table 6. Furthermore, the results are shown in Fig. 19. The elastic parameters inversion performance of the ML algorithms is relatively poor.

The prediction results are subjected to quantitative analysis to compare the performance of the O-SHADE algorithm with that of several ML algorithms. The evaluation of the O-SHADE algorithm is based on the absolute value of the relative error, whereas the ML algorithms are evaluated using the mean absolute percentage error (MAPE) as per the equation presented below.

$$\mathrm{MAPE} = \frac{100}{n}\sum_{i=1}^{n} |A_i - F_i|/A_i \tag{49}$$

where: n - the size of the validation set.

The results are shown in Table 7. In conclusion, for IDSA, the performance of the O-SHADE algorithm is much better than that of the ML algorithms.

5. Numerical experiment of elastic parameter inversion

5.1. Simulation scheme

The numerical model is established in ABAQUS, as shown in Fig. 14. The parameters of sensing casing and cement sheath and relative parameters are listed in Table 8.

Sandstone and shale were utilized to assess the performance of O-SHADE. Table 9 demonstrates the range of orthotropic elastic parameters and corresponding actual values (Gui et al., 2019; Li et al., 2011). Isotropic elastic is a special case of orthotropic elastic. A successful inversion of orthotropic elastic parameters indicates that O-SHADE will perform well in the inversion of isotropic elastic parameters.

5.2. Results

Fig. 20 and Table 10 display the outcome of inverting orthotropic elastic parameters. The inversion test achieved the required

accuracy for sandstone and shale after 676 and 1,733 iterations. The precision of the results is relatively high, signifying the efficacy of the O-SHADE algorithm in inverting elastic parameters.

6. Discussion

This paper provides a comprehensive account of the IDSA, including its basic theory and technical details. To begin, we explore the deformation behavior of rock mass in the DSA theory, with particular attention to micro-fractures surrounding the wellbore. Our investigation reveals that these micro-fractures become over-compressed after the wellbore is formed, a finding supported by Ref. (Zhang and Chen, 2022). Building on this, we establish the IPM to describe the deformation behavior of these micro-fractures. We also propose a method to convert strain components into the axial strain of fiber optics, which enables the calculation of in-situ stress using elastic parameters of the rock mass. Finally, we present the O-SHADE algorithm based on the SHADE algorithm and the ABAQUS. By substituting fiber optic strain data measured by IPM into the O-SHADE algorithm, we can invert the formation's elastic parameters.

The implementation of IPM induces micro-fracture expansion around the wellbore, with varying degrees of expansion due to location-specific stress states (Zhang and Chen, 2022), leading to orthotropic and anisotropic rock mass properties. Micro-fractures fully expand at a certain pressure threshold, resulting in an orthotropic and homogeneous rock mass, with pressure-induced micro-fracture changes having minimal impact.

The O-SHADE algorithm faces several challenges that need attention. One critical issue is the requirement to specify the approximate range of elastic parameters. A broad parameter range may lead to slow convergence, while a narrow range may result in the algorithm failing to converge to the actual value. The elastic modulus interval significantly impacts algorithm performance, with a recommended limit of 15 GPa for optimal results. The target area rock mass elastic modulus should be measured to obtain the elastic modulus distribution range. However, the computational cost of the O-SHADE algorithm is relatively high.

Assigning elastic parameters as field variables and using a distributed algorithm structure are recommended to enhance the computational efficiency and accuracy of the algorithm. These modifications can reduce the time consumed by ABAQUS startup and encapsulation, significantly improving the algorithm's performance while reducing computational costs.

Due to the lack of data on actual fiber optic strain, the results can only prove the feasibility of the IDSA theory however, even though many types of research on strain measurement with fiber optics (Kwon et al., 2018; Schenato et al., 2018), the feasibility of strain measurement with sensing casing has not been studied. For example, the strain conductivity coefficient between the fiber optic and the sensing casing is not always one hundred percent. So, it needs to be corrected. In addition, the macro bending loss of fiber optics is not considered, which will affect the structure of the sensing casing.

The IDSA model relies on a series of assumptions, which can limit the accuracy of measurements taken using this method in highly anisotropic formations, as well as in formations that exhibit high plasticity or creep or in sections where wellbore stability is poor. In order to enhance the applicability of the IDSA method for different types of formations, it is important to develop corresponding modification methods. As mentioned above, the spatial resolution of in-situ stress measurement can be improved. Due to the high spatial resolution of fiber optic strain sensing, many measurement results can be obtained in a single measurement. In this study, twenty-seven sensing points are measured. However, there are only twelve elastic parameters. Therefore, in theory, only twelve adjacent sensing points are needed to measure the in-situ stress. Hence, the relative algorithms are needed to be studied in the future.

Additionally, the measurement of dynamic stress has not yet been achieved. Measuring dynamic stress is relatively less difficult than in-situ stress due to the presence of dynamic strain in the sensing object itself. The strain changes sensed by the sensing casing can be solved using the analytical or numerical models established in this paper and combined with the measurement results of in-situ stress and formation elastic parameters to achieve dynamic monitoring of in-situ stress.

The above issues will be studied and elaborated on in the other parts of the series of papers to modify and refine the method.

7. Conclusions

The primary objective of this study is to present a novel method for measuring in-situ stress utilizing fiber optics. This method can have high spatial resolution and long-term monitoring of in-situ stress. The main conclusions of this study are as follows.

(1) The feasibility of the IDSA method has been preliminarily confirmed, and the method can be utilized for measuring in-situ stress and elastic parameters.
(2) After the borehole is formed, the micro-fractures around the well are over-compressed. During the IPM testing, the rock mass will go through three states: linear isotropic, nonlinear anisotropic, and linear orthotropic.
(3) The IDSA fitness function is multimodal, and the O-SHADE algorithm can accurately invert the rock mass orthotropic elastic parameters. The O-SHADE algorithm demonstrates better inversion accuracy than others and can even invert three-dimensional orthotropic elastic parameters.

CRediT authorship contribution statement

Kun-Peng Zhang: Conceptualization, Data curation, Formal analysis, Investigation, Methodology, Project administration, Resources, Software, Supervision, Validation, Visualization, Writing – original draft, Writing – review & editing. **Mian Chen:** Conceptualization, Data curation, Formal analysis, Funding acquisition, Methodology, Project administration, Supervision, Writing – review & editing. **Chang-Jun Zhao:** Data curation, Formal analysis, Writing – original draft, Writing – review & editing. **Su Wang:** Data curation, Formal analysis, Software. **Yong-Dong Fan:** Software, Validation, Visualization.

Declaration of competing interest

The authors declare that they have no known competing financial interests or personal relationships that could have appeared to influence the work reported in this paper.

Acknowledgements

The authors are grateful for the Project Support of NSFC (No. U19B6003-05 and No. 52074314).

Nomenclature

Abbreviations

DE	Differential Evolution algorithm
DSA	Differential Strain Analysis

GBDT	Gradient Boosted Decision Tree
GSP	Generalized Schwefel's Problem
IDSA	Inverse Differential Strain Analysis
IPM	Internal Pressurizing Method
MAPE	Mean Absolute Percentage Error
ML	Machine Learning
O-SHADE	Orthotropic-SHADE
RT	Regression Tree
SHADE	Success-History based parameters Adaptation for Differential Evolution algorithm

Symbols

A	External archive
A_i	Actual value
$\boldsymbol{c_i}$	Cohesion
$\boldsymbol{CR_i^t}$	Crossover rate
D	Dimensional of the problem
E	Rock matrix elastic modulus
E_c	Sensing casing elastic modulus
E_s	Cement sheath elastic modulus
E_i	Orthotropic elastic modulus
$\boldsymbol{f_i}$	Friction coefficient
F_i	Predicted value
$\boldsymbol{F_i^t}$	Scaling factor
G	Shear modulus of the matrix
K_n	Fracture normal stiffness
G_{ij}	Orthotropic shear modulus
K_{n0}	Fracture initial normal stiffness
K_s	fracture shear strength
K_{s0}	Fracture initial shear strength
l_i, m_i, n_i	Direction cosine
L	Side length of rock mass unit in DSA
M	The number of sensing points
MAX	The maximum value of loci
$\boldsymbol{M_{F,r_i}}$	Controlling factor of scaling factor
$\boldsymbol{M_{CR,r_i}}$	Controlling factor of crossover rate
MIN	The minimum value of loci
n	Size of the validation set
N	Population size
N_f	The number of micro-fractures
$\boldsymbol{N_i}$	Coordinate base vectors of the fracture's local coordinate system
P_0	hydrostatic pressure or internal pressure
R	Cylinder radius
R_c	A positive constant close to 1
S_i	Fracture surface area
S_{CR}	Archive of crossover rate
S_F	Archive of scaling factor
$\lvert\boldsymbol{S_F}\rvert$	Size of scaling factor archive
$[\boldsymbol{S}]_{xyz}$	The material matrix in the global coordinate system
$[\boldsymbol{S}]_{123}$	The material matrix in the local coordinate system
$\mathbf{T}$	Normalized fiber optic axial tangent vector
$[\boldsymbol{T}]$	Conversion matrix
$\boldsymbol{u_{j,i}^t}$	Crossed gene
$\boldsymbol{U_i^t}$	Crossed individual
$\boldsymbol{v_{j,i}^t}$	Mutated gene
V	Rock mass unit volume
$\mathbf{V}$	Fiber optic axial tangent vector
V_i	Mutant individual
$\boldsymbol{w}$	The fitness value of orthotropic elastic parameter inversion problem
$\boldsymbol{w_s}$	The fitness value of GSP
$\boldsymbol{w_k}$	Individual's weight
$\boldsymbol{x_{d,i}^t}$	Original gene
$\boldsymbol{X_{pbest}^t}$	Individual's personal best
$\boldsymbol{X_i^t}$	Individual
$\boldsymbol{\alpha_f}, \boldsymbol{\beta_f}, \boldsymbol{\gamma_f}$	Fracture dip angles
β_m	Matrix effective compression coefficient
δ_i	Fracture total displacement
$\boldsymbol{\delta_n^i}$	Fracture normal displacement
$\boldsymbol{\delta_s^i}$	Fracture shear displacement
$\boldsymbol{\varepsilon_{ij}}$	Rock mass strain components
$\boldsymbol{\varepsilon_1^s} \sim \boldsymbol{\varepsilon_9^s}$	Strains measured by strain gauges in DSA
$\boldsymbol{\varepsilon_{ij}^{DSA}}$	Rock mass strain in DSA
$\boldsymbol{\varepsilon_{ij}^m}$	Matrix strain
$\boldsymbol{\varepsilon_{ij}^f}$	Micro-fracture strain
$\boldsymbol{\varepsilon_{11}}$, $\boldsymbol{\varepsilon_{22}}$, $\boldsymbol{\varepsilon_{33}}$	Principal strains
$\boldsymbol{\varepsilon_N}$	Tangential strain along the fiber optic axis
$\boldsymbol{\theta}$	Polar angle
σ_n	Fracture normal stress
σ_{nmax}	Fracture maximum normal stress
σ_s	Fracture shear stress
$[\boldsymbol{\sigma}]_{DSA}$	Stress matrix of rock mass in DSA
$\boldsymbol{\sigma_{ij}^I}$	Released in-situ stress state components
$\boldsymbol{\sigma_{11}}$, $\boldsymbol{\sigma_{22}}$, $\boldsymbol{\sigma_{33}}$	Principal stresses
$\boldsymbol{\tau_p^i}$	Shear strength
$\boldsymbol{\tau_s}$	Shear stress
υ	Poisson's ratio of the rock mass matrix
υ_c	Sensing casing elastic modulus
υ_s	Cement sheath Poisson's ratio
υ_{ij}	Orthotropic Poisson's ratio
$\boldsymbol{\varphi}$	Helix angle

References

Alabdullah, A.A., Iqbal, M., Zahid, M., Khan, K., Amin, M.N., Jalal, F.E., 2022. Prediction of rapid chloride penetration resistance of metakaolin based high strength concrete using light GBM and XGBoost models by incorporating SHAP analysis. Construct. Build. Mater. 345, 128296. https://doi.org/10.1016/j.conbuildmat.2022.128296.

Alhemdi, A., Gu, M., 2022. Method to account for natural fracture induced elastic anisotropy in geomechanical characterization of shale gas reservoirs. J. Nat. Gas Sci. Eng. 101, 104478. https://doi.org/10.1016/j.jngse.2022.104478.

Alnahit, A.O., Mishra, A.K., Khan, A.A., 2022. Stream water quality prediction using boosted regression tree and random forest models. Stoch. Environ. Res. Risk Assess. 36, 2661–2680. https://doi.org/10.1007/s00477-021-02152-4.

Carbillet, L., Heap, M.J., Baud, P., Wadsworth, F.B., Reuschlé, T., 2022. The Influence of grain size distribution on mechanical compaction and compaction localization in porous rocks. J. Geophys. Res. Solid Earth 127, 1–22. https://doi.org/10.1029/2022JB025216.

Chao, L., 2021. Improvement Strategies for Particle Swarm Optimization Algorithms with. Applications. Jiangnan University. https://doi.org/10.27169/d.cnki.gwqgu.2021.001930 (in Chinese).

Chen, M., Zhang, Y., Jin, Y., Li, L., 2009. Experimental study of influence of loading rate on Kaiser effect of different lithological rocks. Chin. J. Rock Mech. Eng. 28, 2599–2604 (in Chinese).

Chen, T., He, T., Benesty, M., Khotilovich, V., Tang, Y., Cho, H., Chen, K., Mitchell, R., Cano, I., Zhou, T., 2015. Xgboost: extreme gradient boosting. R Packag. version 0.4-2. 1 (4), 1–4.

Clough, G.W., Duncan, J.M., 1978. Finite element analysis of retaining wall behavior. J. Soil Mech. Found. 12, 1657–1673. https://doi.org/10.1061/JSFEAQ.0001713.

Cong, Z., Li, Y., Pan, Y., Liu, B., Shi, Y., Wei, J., Li, W., 2022. Study on CO_2 foam fracturing model and fracture propagation simulation. Energy 238, 121778. https://doi.org/10.1016/j.energy.2021.121778.

Cornet, F.H., Valette, B., 1984. In situ stress determination from hydraulic injection test data. J. Geophys. Res. 89, 11527–11537. https://doi.org/10.1029/JB089iB13p11527.

Emery, C.L., 1962. The Measurement of Strains in Mine Rocks, Mining Research. Elsevier.

Fairhurst, C., 1964. Measurement of in-situ rock stresses. With particular reference to hydraulic fracturing. Rock Mech. Eng. Geol. 2, 129–134.

Fan, Y., Jin, Y., Pang, H., Wang, S., 2022. Enhanced rate of penetration prediction with rock drillability constraints: a machine learning approach. In: 56th US Rock Mechanics/Geomechanics Symposium. American Rock Mechanics Association, Santa Fe. https://doi.org/10.56952/ARMA-2022-0375.

Friedman, J.H., 2001. Greedy function approximation: a gradient boosting machine. Ann. Stat. 1189–1232. https://doi.org/10.1214/AOS%2F1013203451.
Froggatt, M., Moore, J., 1998. High-spatial-resolution distributed strain measurement in optical fiber with Rayleigh scatter. Appl. Opt. 37, 1735–1740. https://doi.org/10.1364/AO.37.001735.
Ge, W., Zhang, F., Chen, M., Jin, Y., Lu, Y., Hou, B., 2015. Research on geotress measurement using DRA-Kaiser method in salt-gypsum formation. Chin. J. Rock Mech. Eng. 34, 3138–3142. https://doi.org/10.13722/j.cnki.jrme.2014.0132.
Gray, D., Anderson, P., Logel, J., As, T.E.N., Delbecq, F., Schmidt, D., 2010. Principle stress estimation in shale plays using 3D seismic. GeoCanada 36, 38–43. https://api.semanticscholar.org/CorpusID:56473790.
Gray, D., Anderson, P., Logel, J., Delbecq, F., Schmidt, D., Schmid, R., 2012. Estimation of stress and geomechanical properties using 3D seismic data. First Break 30, 59–68. https://doi.org/10.3997/1365-2397.2011042.
Gray, F.D., 2013. Methods and Systems for Estimating Stress Using Seismic Data. U.S. Patent. No 861950.
Gray, F.D., Anderson, P.F., Logel, J., Delbecq, F., Schmidt, D., 2010a. Estimating in-situ, anisotropic, principal stresses from 3D seismic. In: 72nd EAGE Conference and Exhibition Incorporating SPE EUROPEC 2010. European Association of Geoscientists & Engineers, Barcelona, pp. 155–161. https://doi.org/10.3997/2214-4609.201400910.
Gray, F.D., Schmidt, D.P., Delbecq, F., 2010b. Optimize shale gas field development using stresses and rock strength derived from 3D seismic data. In: Canadian Unconventional Resources and International Petroleum Conference. Society of Petroleum Engineers (SPE), Calgary, pp. 1–9. https://doi.org/10.2118/137315-MS.
Gui, J., Chen, P., Ma, T., 2019. The spatial distribution of elastic parameters of orthotropic rocks. J. Southwest Pet. Univ. Sci. Technol. Ed. 41, 13–28. https://doi.org/10.11885/j.issn.1674-5086.2018.09.21.02 (in Chinese).
Haimson, B.C., Cornet, F.H., 2003. ISRM suggested methods for rock stress estimation—part 3: hydraulic fracturing (HF) and/or hydraulic testing of pre-existing fractures (HTPF). Int. J. Rock Mech. Min. Sci. 40, 1011–1020. https://doi.org/10.1016/j.ijrmms.2003.08.002.
Hast, N., 1967. The state of stresses in the upper part of the earth's crust. Eng. Geol. 2, 5–17. https://doi.org/10.1016/0013-7952(67)90002-6.
Hayashi, K., Abe, H., 1984. A new method for the measurement of in situ stress in geothermal fields. J. Geotherm. Res. Soc. Japan 6, 203–212. https://doi.org/10.11367/grsj1979.6.203.
He, B.G., Hatzor, Y.H., 2015. An analytical solution for recovering the complete in-situ stress tensor from Flat Jack tests. Int. J. Rock Mech. Min. Sci. 78, 118–126. https://doi.org/10.1016/j.ijrmms.2015.05.007.
Hu, W., Li, Z., 2007. Simpler and more effective particle swarm optimization algorithm. J. Softw. 18, 861–868. https://doi.org/10.1360/jos180861 (in Chinese).
Hughson, D.R., Crawford, A.M., 1986. Kaiser effect gauging: a new method for determining the pre-existing in-situ stress from an extracted core by acoustic emissions. In: ISRM International Symposium. ISRM, 1986. p. ISRM-IS-1986-037.
Ito, T., Evans, K., Kawai, K., Hayashi, K., 1999. Hydraulic fracture reopening pressure and the estimation of maximum horizontal stress. Int. J. Rock Mech. Min. Sci. 36, 811–826. https://doi.org/10.1016/S0148-9062(99)00053-4.
Ito, T., Igarashi, A., Kato, H., Ito, H., Sano, O., 2006. Crucial effect of system compliance on the maximum stress estimation in the hydrofracturing method: theoretical considerations and field-test verification. Earth Planets Space 58, 963–971. https://doi.org/10.1186/BF03352601.
Iverson, W.P., 1995. Closure stress calculations in anisotropic formations. In: Low Permeability Reservoirs Symposium. Society of Petroleum Engineers (SPE), Denver. https://doi.org/10.2118/29598-MS.
Kennedy, J., Eberhart, R., 1995. Particle swarm optimization. In: Proceedings of ICNN'95-International Conference on Neural Networks. IEEE, Perth, pp. 1942–1948. https://doi.org/10.1109/ICNN.1995.488968.
Kordell, J., Yu, M., Dasgupta, A., 2022. A fiber optic conjugate stress sensor for instantaneous tangent modulus detection targeting prognostic health monitoring applications. Smart Mater. Struct. 31, 75001. https://doi.org/10.1088/1361-665X/ac6bd2.
Kuriyagawa, M., Kobayashi, H., Matsunaga, I., Yamaguchi, T., Hibiya, K., 1989. Application of hydraulic fracturing to three-dimensional in situ stress measurement. Int. J. Rock Mech. Min. Sci. Geomech. Abstr. 26, 587–593. https://doi.org/10.1016/0148-9062(89)91439-3.
Kwon, Y.S., Seo, D.C., Choi, B.H., Jeon, M.Y., Kwon, I.B., 2018. Strain measurement distributed on a ground anchor bearing plate by fiber optic OFDR sensor. Appl. Sci. 8, 1–10. https://doi.org/10.3390/app8112051.
Leeman, E.R., Hayes, D.J., 1966. A technique for determining the complete state of stress in rock using a single borehole. In: 1st ISRM Congress. International Society for Rock Mechanics and Rock Engineering, Lisbon.
Li, E., Gao, Z., 2022. Particle swarm optimization algorithm with improved particle velocity and position update formula. J. Nanjing Norm. Univ. Nat. Sci. Ed. 45, 118–126. https://doi.org/10.3969/j.issn.1001-4616.2022.01.017.
Li, J., Liu, G., Chen, M., 2011. New model for stress of borehole surrounding rock in orthotropic formation. Chin. J. Rock Mech. Eng. 30, 2481–2485 (in Chinese).
Li, Y., Long, M., Tang, J., Chen, M., Fu, X., 2020. A hydraulic fracture height mathematical model considering the influence of plastic region at fracture tip. Petrol. Explor. Dev. 47, 184–195. https://doi.org/10.1016/S1876-3804(20)60017-9.
Lu, Y., Chen, M., Jin, Y., Pan, D., Hou, B., 2011. Experimental study on stress measurement for sound emission in carbonate formation. Chin. J. Geotech. Eng. 33, 1192–1196 (in Chinese).
Mayer, A., Habib, P., Marchand, R., 1951. Underground rock pressure testing. In: Proceedings of the International Conference on Rock Pressure and Support in Workings. Int. Soc. Rock Mech., Liège, p. 53.
Morgan, J.N., Sonquist, J.A., 1963. Problems in the analysis of survey data, and a proposal. J. Am. Stat. Assoc. 58, 415–434. https://doi.org/10.1080/01621459.1963.10500855.
Rainer, S., Kenneth, P., 1997. Differential evolution-a simple and efficient heuristic for global optimization over continuous spaces. J. Global Optim. 11, 341–359. https://doi.org/10.1023/A:1008202821328.
Schenato, L., Pasuto, A., Galtarossa, A., Palmieri, L., 2018. On the use of OFDR for high-spatial resolution strain measurements in mechanical and geotechnical engineering. In: 2018 IEEE International Instrumentation and Measurement Technology Conference (I2MTC). IEEE, Houston, pp. 1–6. https://doi.org/10.1109/I2MTC.2018.8409772.
Serdyukov, S.V., Kurlenya, M.V., Patutin, A.V., 2016. Hydraulic fracturing for in situ stress measurement. J. Min. Sci. 52, 1031–1038. https://doi.org/10.1134/S1062739116061563.
Shi, L., Zhang, X., Jin, Y., Chen, M., 2004. New method for measurement of in-situ stresses at great depth. Chin. J. Rock Mech. Eng. 23, 2355–2358 (in Chinese).
Sun, J., Palade, V., Wu, X.-J., Fang, W., Wang, Z., 2013. Solving the power economic dispatch problem with generator constraints by random drift particle swarm optimization. IEEE Trans. Ind. Inf. 10, 222–232. https://doi.org/10.1109/TII.2013.2267392.
Tanabe, R., Fukunaga, A., 2013. Success-history based parameter adaptation for differential evolution. In: Proceedings of the IEEE Congress on Evolutionary Computation. IEEE, Cancun, Mexico, pp. 71–78. https://doi.org/10.1109/CEC.2013.6557555.
Walsh, J.B., 1965. The effect of cracks on the compressibility of rock. J. Geophys. Res. 70, 381–389. https://doi.org/10.1029/JZ070i002p00381.
Wang, X.H., Li, J.J., 2004. Hybrid particle swarm optimization with simulated annealing. In: Proceedings of 2004 International Conference on Machine Learning and Cybernetics. IEEE, Shanghai, pp. 2402–2405. https://doi.org/10.1109/ICMLC.2004.1382205.
Weng, Y., Paal, S.G., 2022. Machine learning-based wind pressure prediction of low-rise non-isolated buildings. Eng. Struct. 258, 114148. https://doi.org/10.1016/j.engstruct.2022.114148.
Wong, R.C.K., Schmitt, D.R., Collis, D., Gautam, R., 2008. Inherent transversely isotropic elastic parameters of over-consolidated shale measured by ultrasonic waves and their comparison with static and acoustic in situ log measurements. J. Geophys. Eng. 5, 103–117. https://doi.org/10.1088/1742-2132/5/1/011.
Zeng, B., Huang, D., Ye, S., Chen, F., Zhu, T., Tu, Y., 2019. Triaxial extension tests on sandstone using a simple auxiliary apparatus. Int. J. Rock Mech. Min. Sci. 120, 29–40. https://doi.org/10.1016/j.ijrmms.2019.06.006.
Zhang, G., 2006. Study on Equivalent Orthotropic Mechanical Parameters and Yield Criterion of Jointed Rock Mass and its Engineering Application. Hohai University (in Chinese).
Zhang, G., Jin, Y., Chen, M., 2002. Measurement of in-situ stresses by Kaiser effect under confining pressures. Chin. J. Rock Mech. Eng. 21, 360–363 (in Chinese).
Zhang, J., Li, Y., Pan, Y., Wang, X., Yan, M., Shi, X., Zhou, X., Li, H., 2021. Experiments and analysis on the Influence of multiple closed cemented natural fractures on hydraulic fracture propagation in a tight sandstone reservoir. Eng. Geol. 281, 105981. https://doi.org/10.1016/j.enggeo.2020.105981.
Zhang, K., Chen, M., 2022. Stress distribution of cased elliptical hole with high fluid pressure: analytical expression. J. Pet. Sci. Eng. 208, 109437. https://doi.org/10.1016/j.petrol.2021.109437.
Zhang, K., Chen, M., Zhou, C., Dai, Y., Liu, F., Li, J., 2020. Study of alternating acid fracturing treatment in carbonate formation based on true tri-axial experiment. J. Pet. Sci. Eng. 192, 107268. https://doi.org/10.1016/j.petrol.2020.107268.
Zhang, K., Hou, B., Chen, M., Zhou, C., Liu, F., 2022. Fatigue acid fracturing: a method to stimulate highly deviated and horizontal wells in limestone formation. J. Pet. Sci. Eng. 208, 109409. https://doi.org/10.1016/j.petrol.2021.109409.
Zheng, X., Shi, B., Zhang, C.C., Sun, Y., Zhang, L., Han, H., 2021. Strain transfer mechanism in surface-bonded distributed fiber-optic sensors subjected to linear strain gradients: theoretical modeling and experimental validation. Meas. J. Int. Meas. Confed. 179, 109510. https://doi.org/10.1016/j.measurement.2021.109510.